




Magnetic control over the fundamental structure of atomic wires

Sudipto Chakrabarti¹, Ayelet Vilan ¹, Gai Deutch¹, Annabelle Oz², Oded Hod ², Juan E. Peralta³ & Oren Tal ¹✉

When reducing the size of materials towards the nanoscale, magnetic properties can emerge due to structural variations. Here, we show the reverse effect, where the structure of nanomaterials is controlled by magnetic manipulations. Using the break-junction technique, we find that the interatomic distance in platinum atomic wires is shorter or longer by up to ~20%, when a magnetic field is applied parallel or perpendicular to the wires during their formation, respectively. The magnetic field direction also affects the wire length, where longer (shorter) wires are formed under a parallel (perpendicular) field. Our experimental analysis, supported by calculations, indicates that the direction of the applied magnetic field promotes the formation of suspended atomic wires with a specific magnetization orientation associated with typical orbital characteristics, interatomic distance, and stability. A similar effect is found for various metal and metal-oxide atomic wires, demonstrating that magnetic fields can control the atomistic structure of different nanomaterials when applied during their formation stage.

¹Department of Chemical and Biological Physics, Weizmann Institute of Science, Rehovot 7610001, Israel. ²School of Chemistry and The Sackler Center for Computational Molecular and Materials Science, Tel Aviv University, Tel Aviv 6997801, Israel. ³Department of Physics, Central Michigan University, Mt. Pleasant, MI 48859, USA. ✉email: oren.tal@weizmann.ac.il

One of the fascinating aspects of nanostructures is the new magnetic effects that are often developed as the dimensions of materials are reduced to the nanoscale. For example, while bulk gold (Au) is non-magnetic, gold nanoparticles may exhibit a finite magnetization¹, and covering copper (Cu) with a film of C₆₀ molecules can promote a ferromagnetic ordering at the Cu surface². Over the years, structural manipulations that take advantage of the peculiar characteristics of nanomaterials were harnessed to achieve magnetic effects^{3–8}. An interesting question that arises is whether the inverse relation can be realized. Namely, can magnetic manipulations lead to novel structural effects in nanomaterials?

Magneto-structural effects, such as magnetostriction^{9–11} and piezomagnetism^{12–14} are manifested as changes in the dimensions of magnetic materials in response to an applied magnetic field. These effects have diverse scientific and technological implications, either as undesirable effects in accurate measurements and device operation, or as means to achieve mechanical action via magnetic stimuli^{15–18}. Since they are not limited to a specific length-scale, such effects can be observed, in principle, in nanometer-sized materials. However, their magnitude is typically of the order of parts per million, and therefore it is extremely challenging to detect them in nanoscale structures. Given the unique structural properties of nanomaterials, including dominant surface effects, reduced number of bonds between atoms (low atomic coordination), and reduced dimensionality, it is natural to expect the emergence of peculiar magneto-structural effects that are not necessarily revealed in bulk materials. Such

effects, if detected, can shed new light on the physics of nanoscale materials and pave novel ways to control their properties.

In the present study, using the mechanically controllable break-junction technique (Fig. 1a), we show that the magnitude and orientation of applied magnetic fields determine the structural properties of atomic wires during their formation. Specifically, we find that, when platinum (Pt) atomic wires are formed in the presence of an applied magnetic field parallel to the wire's axis, the interatomic distance along the wire is shorter by up to ~20%, reaching a saturation at a magnetic field of about 1.25 T (Tesla). The same field direction also promotes the formation of longer atomic wires. The situation is reversed when a perpendicular magnetic field is applied, leading to a longer interatomic distance by up to ~20%, with saturation at a similar magnetic field strength of about 1.25 T, and the formation of shorter atomic wires. These observations are substantiated by analyzing thousands of atomic wires. A minimal model that considers Zeeman splitting and thermal energy, successfully describes our experimental observations. The model, supported by ab-initio calculations, suggests that the direction of an applied magnetic field promotes the formation of stretched atomic wires with a specific magnetization orientation associated with a characteristic interatomic distance and stability. The microscopic mechanism underlying this behavior is analyzed via further calculations and experiments that identify the central role of spin-orbit coupling (SOC), and show that changes in the magnetization directions lead to variations in orbital occupation accompanied by variations in interatomic binding. Importantly, we further present a similar

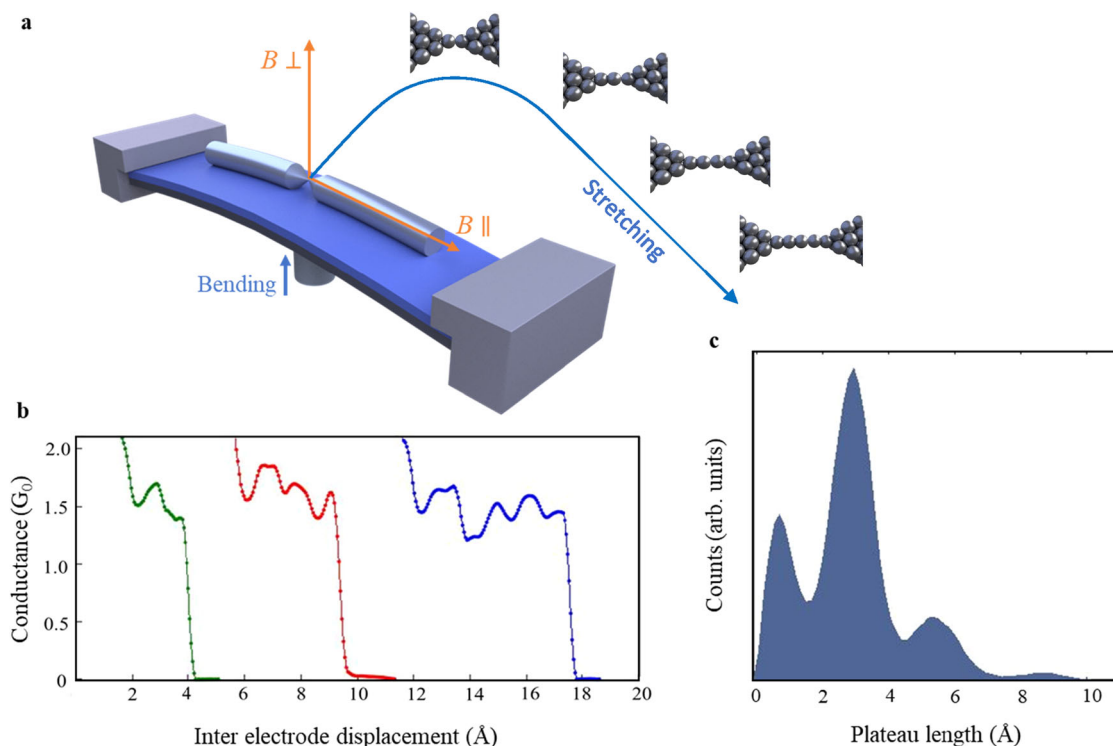


Fig. 1 Formation of Pt atomic wires in a break-junction setup. **a** Illustration of a break-junction setup and sketches of stretched Pt atomic wires. When an atomic contact between the junction's electrodes is stretched, atoms are pulled from the electrode to form an atomic wire. The process can be repeated by remaking and stretching the contact. A magnetic field can be applied parallel or perpendicular to the junction axis (orange arrows) during the formation of atomic wires. **b** Examples of conductance traces as a function of inter electrode displacement measured in the absence of a magnetic field and with a bias voltage of 20 mV. Right before complete junction breaking, the conductance drops to ~1.6 G_0 , the typical conductance of a constriction with a cross-section of one Pt atom between the Pt electrodes (see Supplementary Section 1). Further stretching yields a conductance plateau that ends when the junction breaks. **c** Length histogram composed of 10,000 such conductance traces that presents the number of times that a plateau with a given length was observed in the conductance range of 1.0–2.5 G_0 . The set of peaks is a signature for the formation of atomic wires with different lengths, and the inter-peak distance is a good measure of the interatomic distance^{21,22,29,47,48}.

magneto-structural activity in various metal and metal-oxide atomic wires, suggesting that the discovered magneto-structural effect may emerge in other nanoscale systems. The peculiar nature and magnitude of the revealed effect indicate that the structural characteristics of nanomaterials indeed promote unusual magneto-structural effects that are not found in bulk materials. Our findings thus reveal a previously unknown magneto-structural effect, where magnetic field manipulations at the fabrication stage can dictate the interatomic bonding properties in nanoscale systems. This effect can therefore be used to shape the structural properties of nanomaterials.

Our choice of atomic wires (Fig. 1a) as a testbed for the study of magneto-structural effects in nanoscale materials stems from their structural, magnetic, and electronic properties^{19–35}. Suspended wires with a diameter of a single atom can be fabricated from pure metals^{19–22}, alloys^{23,35}, oxides^{24,31} or metals decorated with molecules^{25,27}, with a length of up to ~ 10 atoms²⁶. These wires have been used extensively to study fundamental aspects of charge, spin, and heat transport at the nanoscale^{22,29–32}. Here, we first focus on suspended Pt wires that can be fabricated in a break-junction setup or a scanning tunneling microscope by stretching an atomic scale contact between two Pt electrodes. During this process, atoms are pulled one by one from the electrodes to form an atomic wire that bridges the two electrodes^{21,22,28,29}. Unlike bulk Pt, which is paramagnetic (yet close to being ferromagnetic according to the Stoner criterion^{30,36–38}), Pt atomic wires have been computationally predicted to turn ferromagnetic upon stretching^{36–42}. In fact, an experimental indication for magnetic activity in Pt wires was given by measurements of a finite magnetoresistance in this system³⁰. Several density functional theory (DFT) based calculations predicted a reduction in the stability of Pt wires when magnetic ordering is included in the calculation^{36–40}. Nevertheless, magnetic field induced structural modifications in atomic wires have never been studied before by either theory or experiment. Historically, the study of magnetism in Pt, has been an active research field for several decades⁴³ with a rich literature on calculations of magnetic effects in Pt (bulk and surface) contaminated by magnetic impurities (e.g., Refs. ^{44–46}).

Results

Our experimental setup (Fig. 1a) allows us to study ensemble properties of Pt atomic wires. To that end, we form thousands of atomic wires and characterize their structure in the presence of constant magnetic fields of different strengths and directions. The Pt atomic wires are fabricated in ultra-clean conditions and cryogenic vacuum (at 5.1 K) between two Pt electrode tips (Fig. 1a), and their conductance, G (i.e., current over voltage), is recorded as a function of inter-electrode displacement²⁹. Figure 1b presents such conductance traces, shifted horizontally for clarity. Right before breaking of the contact between the two beam segments (the electrodes), the conductance drops to approximately $1.6 G_0$ - the typical conductance of a contact with a single Pt atom cross-section^{21,22,29,47}. Increasing the inter-electrode distance can break this contact or pull another atom from one of the electrode apices to form a short atomic wire that bridges the electrodes^{21,22,29,47}. Further stretching may elongate the wire whenever the applied force on the bridging atoms reaches a critical value, at which an additional atom is pulled into the wire (provided that the wire does not break during the process). As seen in Fig. 1b, the elongation process leads to longer conductance plateaus at $\sim 1.6 G_0$ with fine features^{22,29}. These plateaus end when the wire breaks and the conductance drops abruptly to the tunneling regime. By repeated stretching until wire rupture followed by squeezing the electrodes to reform the

contact (thus preparing the system for the next stretching step), we can sequentially fabricate thousands of atomic wires with different number of atoms and study their structural characteristics in the presence of a magnetic field (see Methods and Supplementary section 2).

Figure 1c presents a histogram of the length distribution of the $1.6 G_0$ conductance plateaus that are recorded during 10,000 repeated elongations of the Pt junction. This histogram is constructed by counting the number of times that a given $\sim 1.6 G_0$ plateau length is recorded. The set of peaks in the length histogram seen in Fig. 1c indicates that atomic wires have a high probability to be elongated up to the length of the first peak and then break, or alternatively be elongated up to the length of the second peak and break, etc. This behavior is the fingerprint for the formation of atomic wires with different number of atoms⁴⁸. The inter-peak distance can be considered as a measure of the average interatomic distance along the elongated wire^{21,29,47}. For example, the distance between the third and second peaks, d_{3-2} (Fig. 2a) provides the average difference between the length of the wires associated with the second peak and wires longer by one atom. In the absence of an external magnetic field we find that $d_{3-2} = 2.5 \pm 0.2 \text{ \AA}$ and $d_{2-1} = 2.1 \pm 0.2 \text{ \AA}$. The small difference between d_{3-2} and d_{2-1} is expected in view of previous DFT calculations that showed slightly different interatomic distances for atomic wires of different length^{48,49}. The formation of Pt atomic wires that contain up to 6–7 atoms is experimentally observed but with low abundance^{21,22}. Here, we choose to focus on the shortest (and more abundant) wires that reveal magneto-structural response. This allows for robust data analysis based on large ensembles.

Remarkably, Fig. 2a–c show that the inter-peak distance increases by up to $20.5 \pm 0.6\%$ in response to magnetic field perpendicular to the junction, saturating at a field intensity of about $1.25 T$. In contrast, Fig. 2d–f reveal that the application of a parallel magnetic field leads to an inter-peak distance reduction of $20.5 \pm 0.6\%$ at the most, saturating at a similar magnetic field intensity. These observations indicate a significantly longer interatomic distance along the atomic wires when they are elongated in the presence of a perpendicular magnetic field, and a substantially shorter interatomic distance when a parallel magnetic field is applied during the formation of the wires. Notably, we did not detect any similar magneto-structural response in Au atomic wires (see Supplementary section 4). The insets of Fig. 2g, h, indicate that the most probable conductance of $\sim 1.6 G_0$ is not affected by applied magnetic fields beyond the error bars uncertainty, though subtle conductance variations in the range of $\pm 0.035 G_0$ are found (see Supplementary Section 1).

Next, we examine how the magnitude and orientation of the applied magnetic fields affect the overall length of the formed wires. To that end, we define the length d_{90} as a robust ensemble measure of the formed wire length, such that 90% of the formed wires are shorter than its value (see Supplementary Sections 5 and 6 for an analysis of different methods for wire length evaluation). Figure 2g, h show that a perpendicular magnetic field reduces d_{90} , whereas a parallel magnetic field increases it (see Supplementary Section 7 for the magnetic effect on the number of atoms in the wires). These trends, which are opposite to the interatomic distance dependence on magnetic field, indicate that a perpendicular (parallel) magnetic field increases (decreases) the probability of wire rupture. This, in turn, hints that application of magnetic fields during wire formation influences the relative stability of the elongated wires such that longer (shorter) interatomic distances are correlated with lower (higher) wire endurance towards stretching and thus smaller (larger) overall wire length.

Figure 3 reveals another aspect of the interplay between magnetic field and the structural properties of Pt atomic wires. The

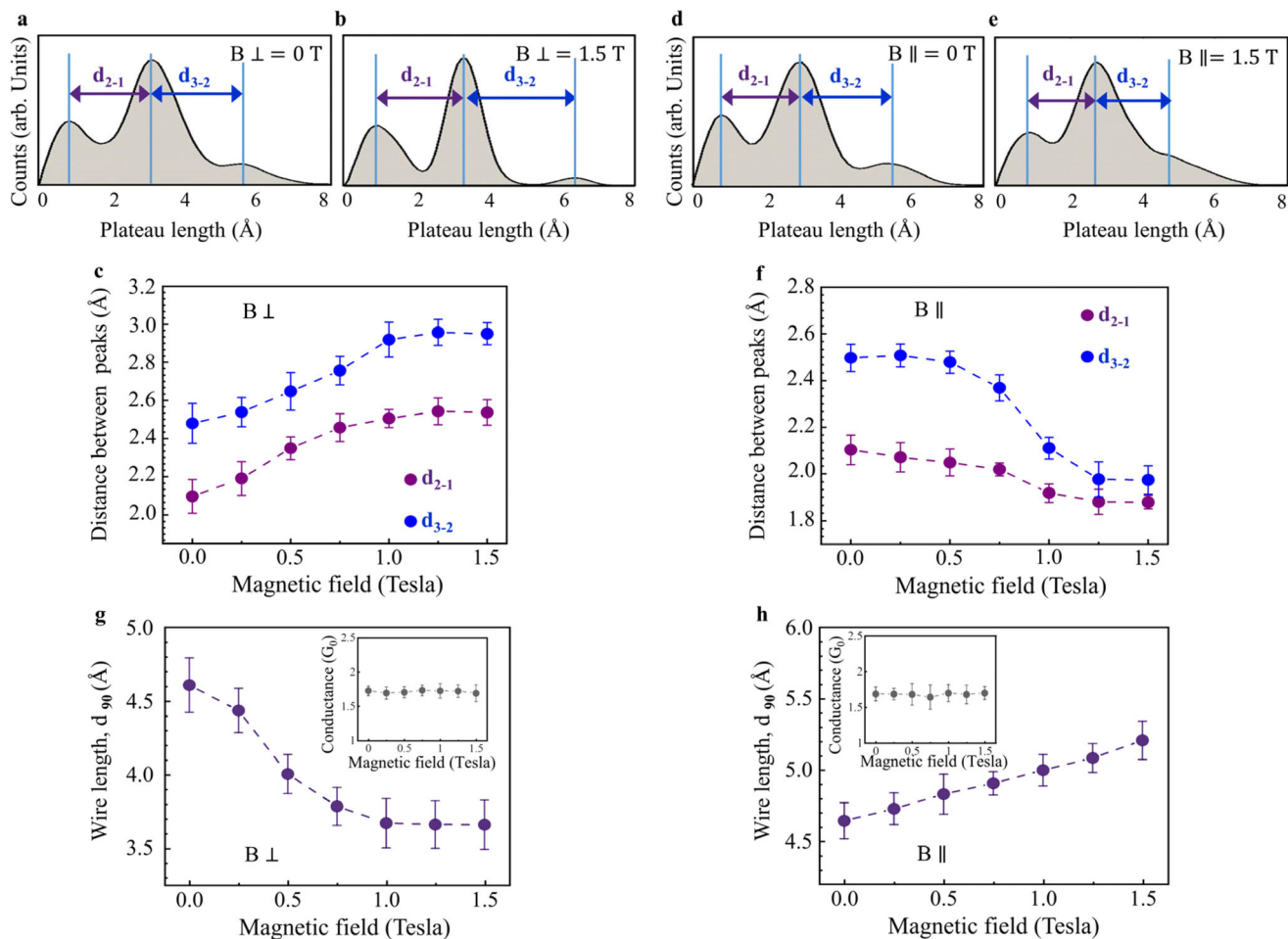


Fig. 2 Magnetic-field-induced structural variations in Pt atomic wires. **a, b** Length histograms formed at zero applied magnetic field and at 1.5 T (Tesla) applied perpendicular to the junction's axis, respectively, as defined in Fig. 1a. d_{2-1} and d_{3-2} are the inter-peak distances, which provide an indication for the average interatomic distance in the elongated wires. **c** Inter-peak distance as a function of perpendicular magnetic field. The overall increase in the inter-peak distance is $20.5 \pm 0.6\%$ for d_{2-1} and $18.9 \pm 0.4\%$ for d_{3-2} . **d, e** Similar to **(a, b)**, but with an applied magnetic field parallel to the junction's axis, as defined in Fig. 1a. **f** Similar to **c**, but with a parallel magnetic field. Here, the overall reduction in the inter-peak distance as a function of parallel magnetic field is $10.5 \pm 0.6\%$ for d_{2-1} and $20.5 \pm 0.6\%$ for d_{3-2} . **g, h** d_{90} , a measure of the wire length, as a function of perpendicular (**g**) and parallel (**h**) magnetic field. Perpendicular (parallel) magnetic fields promote the formation of shorter (longer) wires. Insets: most probable conductance as a function of magnetic field perpendicular and parallel to the junction axis. See Fig. S1 for more details. Overall, fundamental structural properties of the Pt atomic wire are tuned by the direction and strength of the applied magnetic field. The data at each magnetic field in **(c, f, g, h)** is obtained from at least 8 length histograms that were collected during different experimental sessions. Each length histogram is based on 10,000 conductance traces measured under a bias voltage of 20 mV (similar analysis for 100 mV, and 180 mV shows no bias voltage effect, see Supplementary Section 3). The error bars provide the standard deviation of the averaged data.

application of a perpendicular magnetic field (Fig. 3a–h) gives rise to sharper and better resolved peaks in the length histograms, whereas, in the presence of magnetic field parallel to the wires (Fig. 3i–p), wider peaks and relatively blur length histograms are obtained (see detailed analysis in Supplementary Section 8). To explain this, we note that the most frequently formed wires, and hence the most stable ones, tend to break at typical lengths given by the peak centers. In contrast, wires that break at length values between the peak centers are relatively rare and therefore considered to have a less-stable structure, or at least one unstable contact to the electrodes. Therefore, the size of the population of the less-stable configurations (off-peak counts) may serve as a sensitive probe for magnetically induced variations in wire perseverance during elongation. Namely, the peak sharpening (widening) observed with the application of a perpendicular (parallel) magnetic field indicates a reduction (increase) of the wire's endurance during the formation process, in agreement with the analysis presented above (Fig. 2).

To understand the observed magneto-structural effect, we present in Fig. 4a, b schematic curves of the wire's energy as a function of elongation and its first derivative, the corresponding force (wire tension). The required force for breaking a wire is conventionally taken as the maximal force^{40,42}, which corresponds to the inflection point in the energy curve. Our experimental data provide important information on the energy and force curves in the presence of applied magnetic fields. Figures 2c, f show that the distance between peaks is larger under a perpendicular magnetic field and smaller under a parallel field. Recall that the peaks indicate the wire length at which the wires tend to break, and the distance between peaks provides the average interatomic distance in the fully stretched wires^{21,22}. Consequently, Fig. 2c, f reveal that the application of a perpendicular magnetic field promotes wire breaking at a longer interatomic distance, while applied parallel field leads to breaking at a shorter interatomic distance. In the force curves (Fig. 4b), this is manifested as a maximal force position located at a longer length (d_{\perp})

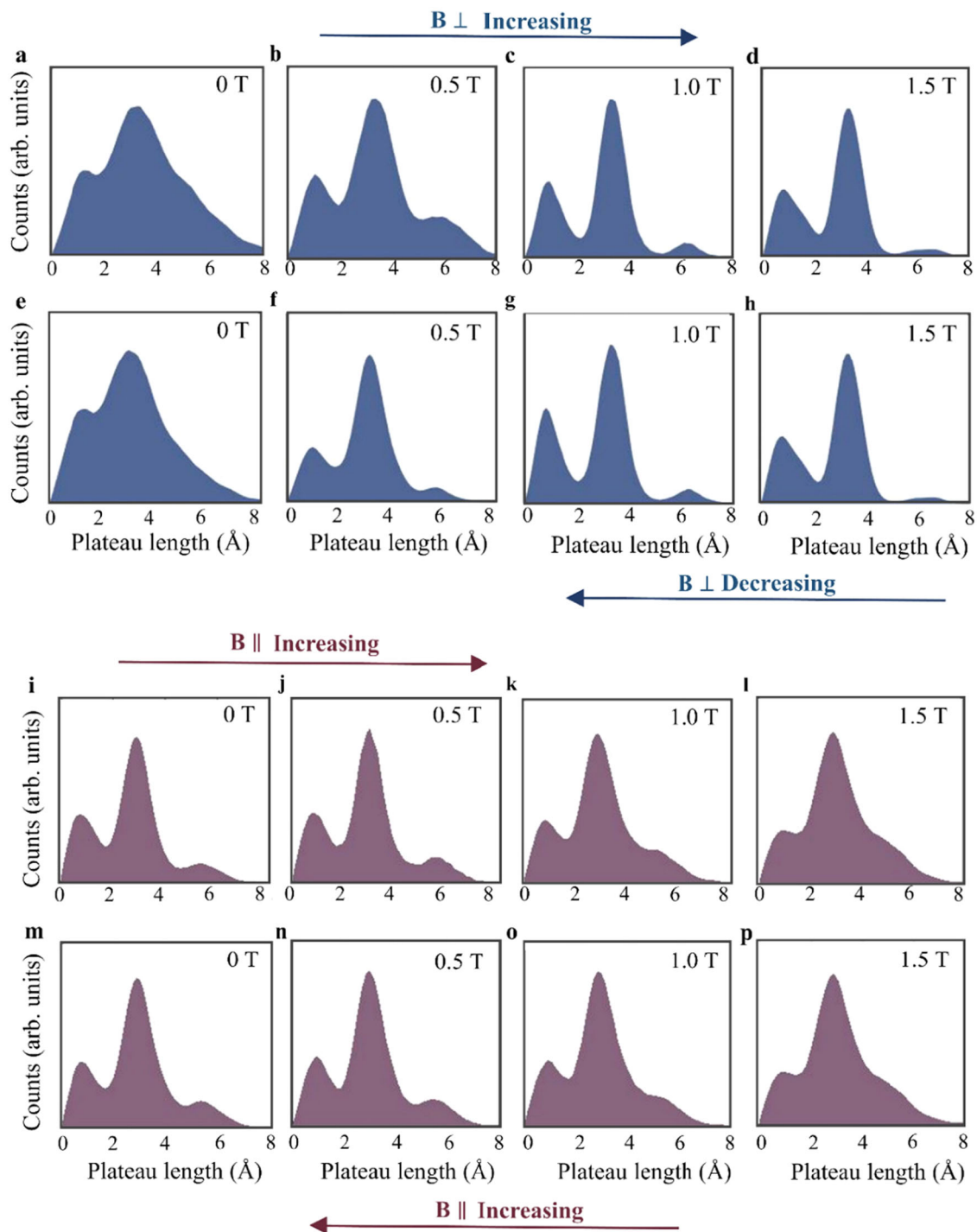


Fig. 3 Magnetic field effect on the less-stable configurations of Pt atomic wires. **a–h** Length histograms based on 10,000 traces recorded consecutively as a function of increasing (**a–d**) and decreasing (**e–h**) magnetic field perpendicular to the junction axis. The peaks' sharpness reversibly increases with the applied magnetic field strength. **i–p** Similar measurements as a function of parallel magnetic field. In contrast to the former case, here the peaks' sharpness decreases reversibly with increasing magnetic field strength. Length histograms with varied sharpness can be obtained at zero magnetic field by using different samples. We deliberately chose histograms with different sharpness to clearly present the (de)sharpening effect. A complementary analysis is presented in Supplementary Section 8, based on histograms of similar zero-field sharpness, allowing for a convenient quantitative comparison. We note that a similar analysis of Au wires control measurements (Supplementary Section 4) reveals no response to parallel magnetic field, whereas a slight increase in the peaks' width is found for a perpendicular field. This effect will be further analyzed elsewhere.

for a perpendicular field and at a shorter length (d_{\parallel}) for a parallel field, with a similar influence on the inflection point of the energy curve (Fig. 4a). Figure 2g, h reveal that the formed wires are shorter when a perpendicular magnetic field is applied and longer

when applying a parallel field. This implies a higher probability of reaching the breaking force under a perpendicular field before reaching the force needed to pull an atom from the electrodes, and vice versa for a parallel applied field. In the force curve

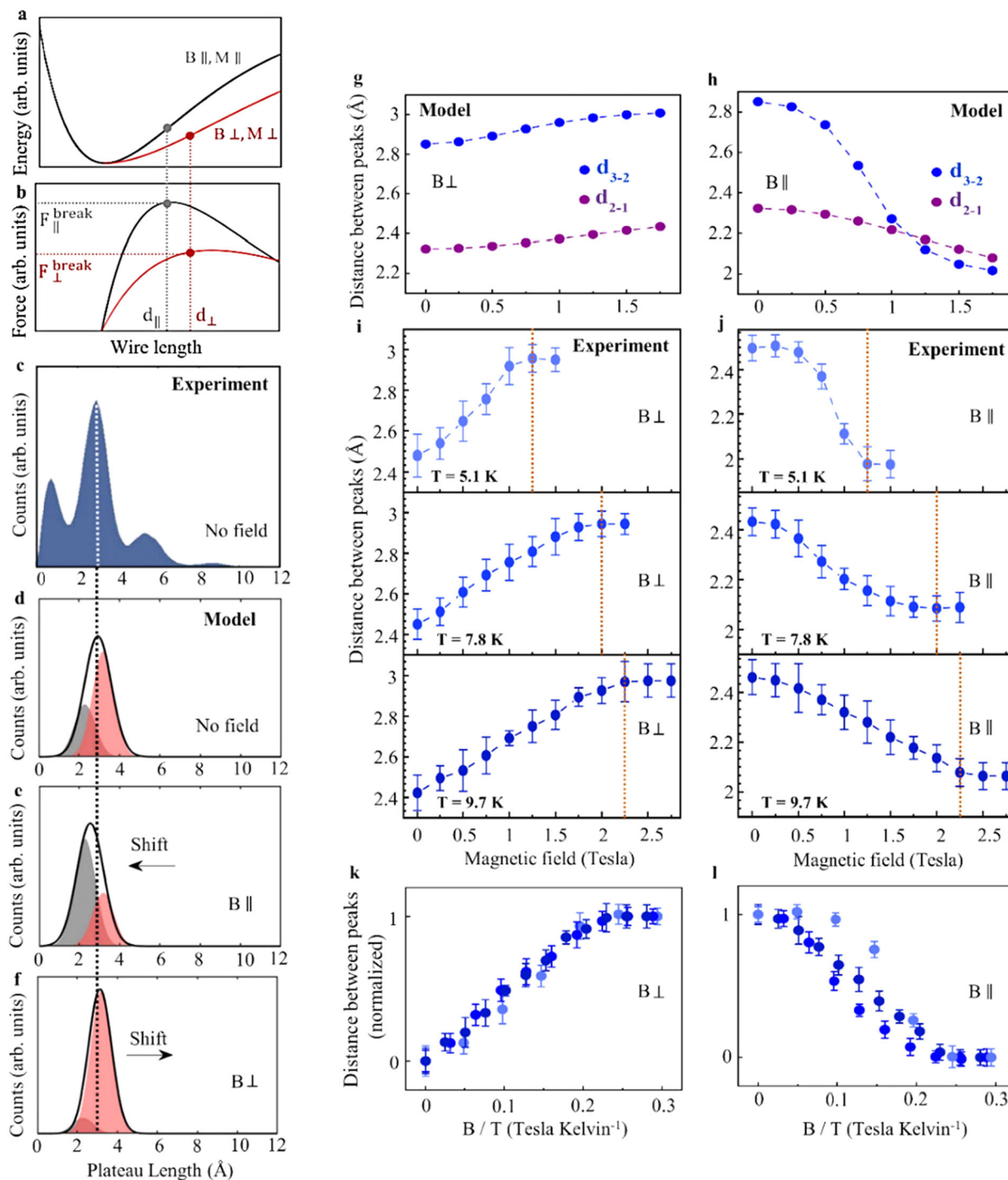


Fig. 4 Minimal model and temperature dependent measurements. **a** Schematic curve of total energy as a function of wire length for parallel and perpendicular magnetic field and magnetization. **b** Same as **(a)** for the force. The breaking force ($F_{\parallel,\perp}^{\text{break}}$) is obtained at different wire length $d_{\parallel,\perp}$ for parallel and perpendicular magnetization and magnetic field orientations. **c** Experimental length histogram at zero magnetic field (same as Fig. 1c) presented for the sake of comparison to our model. **d-f** Illustration of the minimal model: **(d)** At zero magnetic field, two peaks represent the distribution of wire lengths with parallel (gray) and perpendicular (pink) magnetizations. In our model, these distributions are given by similar Gaussians multiplied by Zeeman-based Boltzmann weights that depend on the relative orientations and magnitudes of the magnetization and applied magnetic field. The distributions are centered at d_{\parallel}^n , d_{\perp}^n for the n^{th} peak, and their summed contribution (black envelope) is adapted by setting the Gaussian widths to $\sigma = 0.5 \text{ \AA}$ to fit the experimental peaks in **(c)**. **e** At a finite parallel magnetic field, the two Boltzmann weights are different due to different Zeeman energy for parallel and perpendicular magnetizations. As a result, the heights of the two peaks are different, leading to a down-shift in the position of the maximum of the total distribution (black). **f** The two distributions at finite perpendicular magnetic field. Here, the different Boltzmann weights for parallel and perpendicular magnetizations lead to an up-shift in the position of the maximum of the total distribution (black). **g, h** Calculated d_{2-1} and d_{3-2} as a function of perpendicular **(g)** and parallel **(h)** magnetic field. d_{\parallel}^n , d_{\perp}^n are determined by the onset of saturation in Fig. 2c, f. This model captures the opposite shifts in the inter-peak distance for parallel and perpendicular magnetic fields for both magnetization directions. **i, j** Inter-peak distance as a function of perpendicular **(i)** and parallel **(j)** magnetic field for different temperatures. **k, l** Same as in **(i)**, **(j)**, with magnetic field divided by the temperature.

(Fig. 4b), this is manifested as a lower (higher) maximal force when a perpendicular (parallel) magnetic field is applied, with corresponding variations in the energy curve (Fig. 4a).

Based on the experimental observations, we conclude that the application of parallel or perpendicular magnetic fields during wire fabrication leads to different binding energy characteristics. This can be rationalized in terms of magnetization alignment along the field direction, promoting the formation of wires with magnetization either parallel or perpendicular to their axis. The key point here is that atomic wires with parallel and perpendicular magnetizations have different total energy and force curves as illustrated in Fig. 4a, b. Our non-collinear spin DFT calculations (Supplementary Section 9) qualitatively support this picture by showing that the energy and force curves of stretched wires are indeed different for parallel and perpendicular wire magnetizations (see Fig. S19). This effect can be ascribed to the large spin-orbit interaction of Pt, as discussed below.

A puzzle remains, however, related to the fact that the Zeeman splitting energy associated with the experimentally applied magnetic fields is of the order of 10^{-4} eV, significantly smaller than the estimated energy difference between the parallel and perpendicular magnetization states in the stretched wire (Fig. S19). However, former observations indicate that after each insertion of an atom to the wire, the built tension and wire stiffness are considerably relaxed^{47,50}. Consequentially, the interatomic distance approaches the equilibrium value. Under these conditions, the magnetization preference is suppressed^{36–38,40–42}, thus facilitating the alignment of the magnetization along the magnetic field. If, upon stretching, an anisotropy barrier develops along with the increase in the energy splitting between parallel and perpendicular magnetization states (Supplementary Section 10), a lock-in of the magnetization orientation results. This picture thus explains how the spin orientation can be dictated by relatively small magnetic fields.

The following minimal model provides insights into the origin of the saturation observed in Fig. 2. Considering an ensemble of atomic wires, in the absence of an applied magnetic field, both wires with parallel and perpendicular magnetization configurations coexist at the experimental temperature of 5.1 K. According to this picture, each peak in the measured length histogram (Fig. 4c) is the sum of two distributions (black envelop in Fig. 4d), which represent the two ensembles of wires with perpendicular (pink; Fig. 4d) and parallel (grey; Fig. 4d) magnetizations. The former ensemble is twice as large as the latter since it consists of two perpendicular magnetization orientations versus one for the parallel orientation. For each peak, these two partially overlapping distributions (too close to be resolved experimentally) are represented by Gaussian functions centered at the breaking lengths for wires with parallel and perpendicular magnetizations (d_{\parallel}^n and d_{\perp}^n , respectively, for the n^{th} peak). The Gaussian widths are chosen as $\sigma = 0.5$ Å, such that their sum matches the experimentally observed histogram peaks in the absence of applied magnetic fields (Fig. 4c).

As discussed above, the application of parallel or perpendicular magnetic fields with respect to the wire's axis alters these populations, favoring magnetization alignment along the field. This effect is accounted for by multiplying the Gaussian distributions by appropriate Boltzmann weights (see Supplementary Section 10). These weights consider the Zeeman energy due to the applied magnetic field parallel or perpendicular to the wire's axis for the two magnetization orientations, as well as the competing thermal energy. We note in passing that apart from the parallel and perpendicular magnetization states other possible spin states, such as nearly anti-ferromagnetic configurations, have a considerably smaller Zeeman energy, and are hence neglected in our analysis. As illustrated in Fig. 4e, the application of a parallel magnetic field

increases the wire population with a parallel magnetization (gray) and suppresses the population with a perpendicular magnetization (pink). This yields a shift in the envelope's peak location (black) towards a shorter plateau length. The situation is inverted for a perpendicular magnetic field, as illustrated in Fig. 4f. According to this model, the shift in the peak location as a function of magnetic field asymptotically approaches saturation when the population of wires with magnetization aligned with the field dominates the peak's locations. At zero temperature the locations of the peaks at saturation are d_{\parallel}^n and d_{\perp}^n for the corresponding field orientations. Therefore, as an input to our model, the locations of the peaks of the experimental length histogram at saturation are chosen as an approximation to d_{\parallel}^n and d_{\perp}^n . Figure 4g, h present the model outcome for the inter-peak distance as a function of a parallel and perpendicular magnetic field strength. The observed shifts are similar to the experimental ones in Fig. 2c, f, with lower amplitudes. Varying the magnetization and Gaussian widths in a physically relevant range does not affect the qualitative results of the model (see Supplementary Section 11). Interestingly, a better agreement with the experimental shift amplitudes can be achieved by considering an average atomic magnetization larger than the value of $2.5 \mu_B$ (μ_B - Bohr magneton) used here based on existing literature^{36–42}.

According to this model, temperature increase should shift the onset of saturation to a higher magnetic field, since it is determined by a competition between the Zeeman and thermal energies. In contrast, the temperature effect on the distance between peaks at saturation should be negligible under our experimental conditions. To validate these model predictions, we present in Fig. 4i, j the experimentally obtained distance between peaks, d_{3-2} , as a function of magnetic field, measured at different temperatures (see Supplementary Section 12). A clear upshift in the saturation field with temperature is indeed observed with no apparent variations in the amplitude of the distance between peaks beyond the experimental uncertainty. Figure 4k, l show that scaling the magnetic field by the temperature yields a similar saturation point for all six curves. These observations support the validity of our model and reveal the effect of moderate temperature variations on the magneto-structural response.

We now turn to examine the microscopic origin of the reported effect. Figure 5 shows calculated charge density isosurfaces for parallel (a, green) and perpendicular (b, yellow) magnetizations for a short Pt atomic wire junction, where no noticeable difference between the two is found at first sight. However, subtracting the charge density for the perpendicular magnetization case from that of the parallel magnetization clearly reveals the difference between the two. The positive component (c, red) can be seen as the added contribution to the charge isosurface when the magnetization changes from a perpendicular to parallel orientation and the negative component (d, blue) is the subtracted component due to the same change in magnetization orientation. The shape of the positive isosurface reveals a dominant contribution from d_{z^2} (z is the wire axis), and the nodes in the negative isosurface indicates dominant contributions from d_{xz} and d_{yz} orbitals. We therefore find an enhanced contribution to the charge distribution of d_{z^2} orbitals, on expense of d_{xz} and d_{yz} orbitals, when the magnetization is changed from perpendicular to parallel orientation. This is correlated with a larger Mayer bond order for the peripheral bonds prone to rupture in the stretched wire: 0.2124 for a parallel magnetization and 0.2084 for a perpendicular magnetization with a numerical error of $\pm 10^{-4}$. The moderate change in the difference between bonding and antibonding states (given by the bond order) is accompanied by a significant difference in the binding force, as seen in Supplementary Fig. S18i. This indicates that near rupture, even mild

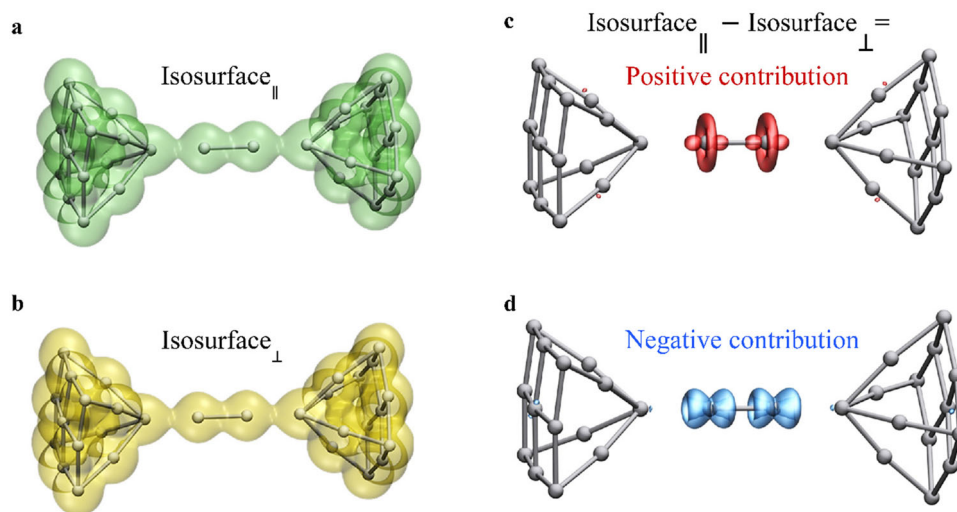


Fig. 5 Calculated spatial distribution of the charge density for a short Pt atomic wire junction. **a, b** Isosurfaces of 1.6 Bohr⁻³ charge density for parallel (**a**; green) and perpendicular (**b**; yellow) magnetizations. **c, d** Isosurfaces of positive (**c**; red) and negative (**d**; blue) charge density differences between the parallel and perpendicular magnetizations isosurfaces. The positive and negative components in (**c, d**) reveal variations in the orbital contribution to the total charge density when changing the magnetization direction.

changes in the bond order may translate to significant variations in the wire tension.

Figure 5 reveals that changes in the spin orientations lead to variations in the orbital characteristics. This is a clear signature of SOC, and an illustration of the link between magnetic-induced manipulations and the resulting structural changes. SOC is not explicitly considered in the above-mentioned phenomenological model but its role can be examined by a comparative experimental analysis, since the unveiled magneto-structural phenomenon is not limited to the case of Pt atomic wires. In fact, iridium (Ir) atomic wires show a similar magneto-structural response as that of Pt (Fig. 6a, b), yet saturating at ~ 3.5 T (compared to ~ 1.25 T for Pt). Considering the almost twice larger magnetic moment in Ir atomic wires than that of Pt wires^{36,39}, one could expect a lower saturation magnetic field for Ir, in contrast to the experimental observations. We suggest that the larger SOC in Pt compared to Ir^{51,52} is the dominant factor that leads to a lower saturation field. In contrast, the lack of magneto-structural response for Au wires (Fig. 6c, d and Supplementary Section 4) indicates that only high SOC is not enough and the effect is not expected in the absence of magnetization, as in the case of Au wires^{36,39}. To further test the role of SOC, we took advantage of the fact that Cu, Ag and Au have a different SOC ($\text{Cu} < \text{Ag} < \text{Au}$)^{51,52}, and repeated our experiments with copper-oxide, silver-oxide, and gold-oxide (CuO, AgO, AuO) atomic wires that can be fabricated when the corresponding metal atomic contacts are exposed to oxygen²⁴ (see Methods). Importantly, suspended CuO, AgO and AuO atomic wires are all expected to develop ferromagnetism with a comparable magnetization^{53–57}. Figure 6e–h show no magneto-structural effect for CuO, and a finite effect for AgO and AuO. These observations indicate that a certain SOC magnitude is required in order to generate the probed magneto-structural effect, and for CuO the involved SOC magnitude is apparently below that threshold. The change in the wire length for AuO and AgO is comparable, but it saturates at different magnetic fields (~ 0.5 T and ~ 1.5 T, respectively). Since the expected magnetizations for AgO and AuO wires are comparable^{53–56} but the SOC of Au is higher, we find that (similar to the case of Pt and Ir) atomic wires with a higher SOC reveal higher structural sensitivity to magnetic field (i.e., lower saturation field). We note that the revealed magneto-structural

response in AgO and AuO atomic wires is a first indication for magnetic activity in such atomic wires, calling for further study of these systems.

Despite the strong magneto-structural effect found in our experiments on Pt atomic wires, we could not find systematic variations in the most probable conductance of these wires as given by conductance histograms (Fig. 2g, h, Insets and Supplementary Section 1). However, this analysis has an uncertainty of ± 0.1 G_0 , thus lower conductance variations cannot be detected. When elongating atomic wires, the conductance oscillates whenever an atom is added into the wire and the stretched linear wire is partially relaxed to a zigzag configuration. These oscillations, which have a typical range of ± 0.05 G_0 , come from variations in the orbital overlap near the Fermi energy^{29,48}. We find that the oscillation amplitude changes by about $+0.035$ G_0 (-0.035 G_0) on average in response to perpendicular (parallel) magnetic fields, (Supplementary Section 1). These observations provide a complementary indication for magnetic field induced variations in the orbital characteristics.

Discussion

The discovered magneto-structural effect is fundamentally different from magnetostriction^{9–11} and piezomagnetism^{12–14}. The latter phenomena are manifested as magnetic field induced variations in the shape of ferromagnetic and antiferromagnetic materials after their formation, due to changes in magnetization orientation. Moreover, these phenomena show hysteretic behavior. In the newly discovered effect, applying a magnetic field during wire formation promotes the fabrication of nanoscale architectures with a specific magnetization orientation and associated structural characteristics that are preserved in the suspended wire. Furthermore, in our measurements hysteresis is neither expected nor observed (Supplementary Section 13). To put the magnitude of the reported effect into context, the structural changes associated with magnetostriction and piezomagnetism are typically in the order of 10^{-2} – $10^{-3}\%$, although larger magnetostriction of $\sim 10^{-1}\%$ was found for specific rare earth transition metal alloys⁵⁸. Minute length variations have also been reported in magnetic exchange force measurements on nickel-oxide substrates, where a height contrast of 0.5–1.5

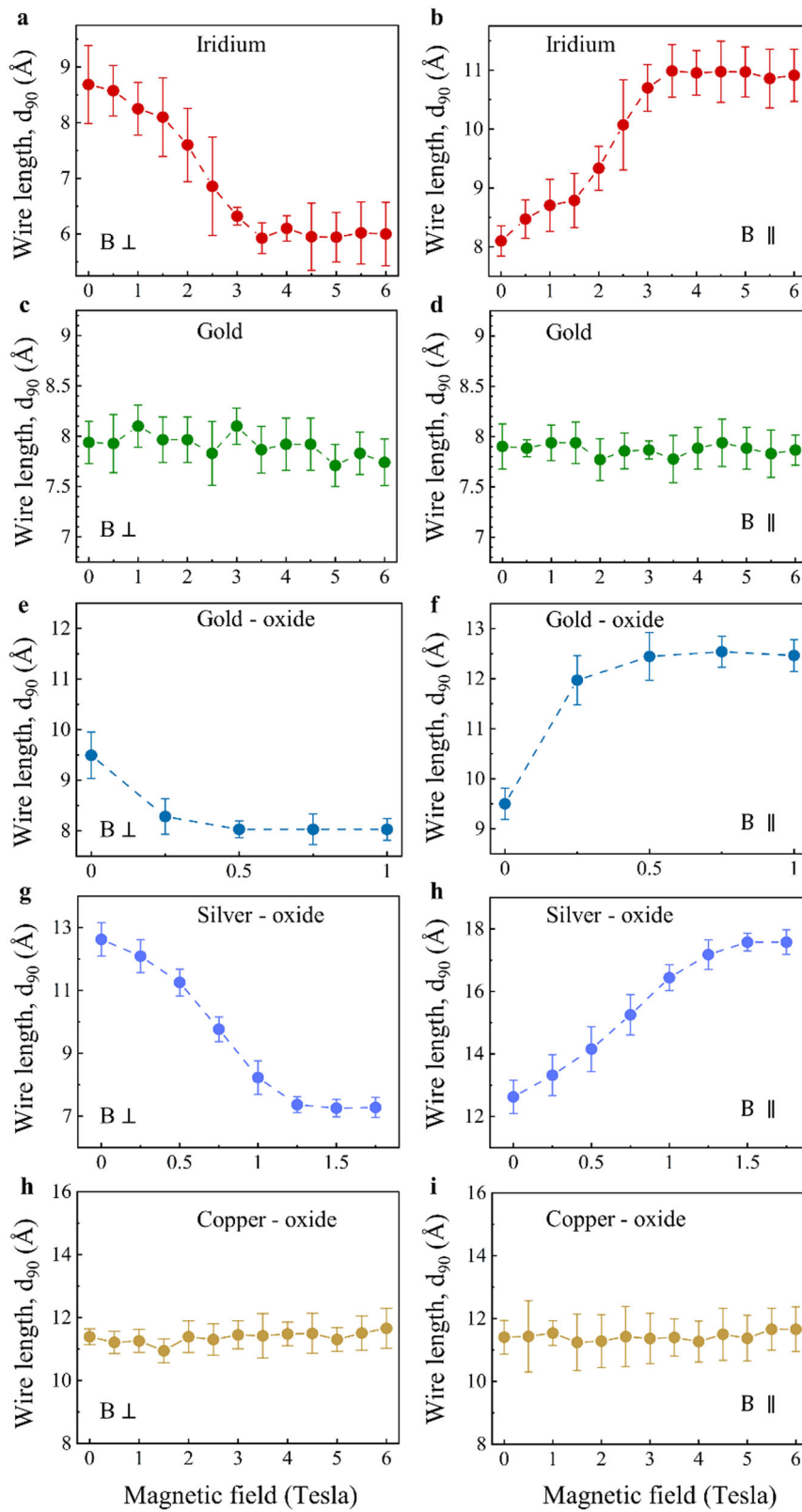


Fig. 6 Magneto-structural effects in different atomic wires. a-i d_{90} as a function of perpendicular (left column) and parallel (right column) magnetic field for iridium (**a, b**), gold (**c, d**), gold-oxide (**e, f**), silver-oxide (**g, h**), and copper-oxide (**h, i**) atomic wires. Each data point provides the average d_{90} obtained from 5 different length histograms of 3000 traces each. Error bars present the standard deviation at each data point.

picometer^{59,60} was at least partially associated with temporary structural relaxation in the scanning tip edge due to an exchange magnetic force, according to DFT calculations (e.g., Refs. ^{61,62}). In contrast, the revealed magneto-structural effect is associated with orders of magnitude larger variations of up to ~20% in the interatomic distance (i.e., ~0.5 Å per interatomic bond).

To conclude, our observations provide a new perspective into the interplay between magnetism and nanoscale material structure, exemplifying that magnetic field direction and magnitude can control the structural properties of nanoscale materials during their formation. The demonstration of the studied magneto-structural effect for several systems, including Pt, Ir, AgO and AuO atomic wires, signifies its generality and indicates that it might be found in other nanoscale systems, possibly possessing sufficiently strong SOC and a sizable magnetization, such as metal and metal-oxide atomic-scale islands on surfaces and magnetically-active molecular junctions.

Methods

Experimental. The experiments are performed using a mechanical controllable break-junction set-up¹⁹ (Fig. 1a). The samples are composed of a notched Pt, Au, Ir Ag or Cu beam (Purity: 99.997%(Pt), 99.998%(Au), 99.9%(Ir), 99.997%(Ag), 99.99999%(Cu) 0.1 mm, 25 mm in length) attached to a flexible bendable substrate made of a 1-mm-thick phosphor-bronze plate covered by 100 μm insulating Kapton film. With the aid of a three-point bending mechanism including a piezoelectric element (PI P-882 PICMA), the substrate is bent to break the wire at its notch in cryogenic vacuum at a base temperature of 5.1 K. Breaking the beam forms a junction with a nanoscale gap between two ultra-clean atomically sharp apices that are used as electrodes. The two apices can be reconnected to have an atomic contact. Elongation of the contact in sub-Å resolution forms an atomic wire (metal-oxide wires are formed only after admitting oxygen into the contact), and the process can be repeated for thousands of times by reforming a multi-atomic contact with conductance of 50–70 G_0 and elongating it to have another atomic wire. Oxygen (99.999%) is introduced to the cold sample via a heated capillary from an external reservoir³¹. The repeated elongation is performed at a rate of 20–40 Hz, while the conductance of the junction is measured simultaneously. The junction is biased with a d.c. voltage provided by a DAQ card (NI-PCI6221). The presented measurements are performed at a bias voltage of 20 mV. The resulting current is amplified by a current preamplifier (Femto amplifier DLPKA 200) and recorded by the DAQ card at a sampling rate of 50–200 kHz. The obtained current values are divided by the applied voltage values to extract the conductance. The inter electrode displacement is found by the exponential dependence of tunneling currents on the separation between the electrodes (see Supplementary Section 2). The magnetic field is applied using a vector superconducting magnet (horizontal ≤3T and vertical ≤9T) that provides a magnetic field parallel or perpendicular to the sample wire. The piezoelectric element that is used to bend the sample is driven by the same DAQ card connected to a piezo driver (Piezomechanik SVR 150/1). The measurements were obtained for five different samples for each metal and three different samples for each metal-oxide, using different cryogenic probes. A similar behavior was found for all measured samples of the same type. The error bars represent the variations between independent measurements, serving as a reliable measure for the degree of experimental uncertainty.

Data analysis. Conductance histograms, length evaluation, and Gaussian fittings are done by in-house MatLab codes. The evaluations of the peak centers and widths in the length histograms are derived by deconvolution into Gaussian peaks using the 'fit.m' MatLab function with 'gauss4' fit type and the 'NonlinearLeastSquares' method. Percentile values (e.g., d_{90}) are derived by the 'prctile.m' function.

Calculations. The underlying assumptions of the minimal model were validated using fully unconstrained non-collinear spin DFT calculations including SOC^{63–65}. All DFT calculations were performed using the Gaussian suite of programs⁶⁶ using the PBEh hybrid density functional approximation^{67–69}, which admixes 25% of orbital-dependent Hartree-Fock exchange with 75% of PBE exchange and 100% PBE correlation, and the Stuttgart-Cologne energy-consistent relativistic (10 electrons) small-core effective core potential, including the spin-orbit component, and the corresponding aug-cc-pVDZ-PP basis-set⁷⁰. Our choice of hybrid functionals is based on their success in treating transition metal complexes and their use in the context of strongly correlated systems^{71,72}. The details of these calculations and the corresponding model systems are provided in Supplementary Section 9.

Data availability

The data that support the findings of this study are available from the corresponding authors upon reasonable request due to the huge volume of the raw data collected in this study.

Code availability

The non-commercial computer codes that support the findings of this study are available from the corresponding authors upon reasonable request.

Received: 15 May 2022; Accepted: 17 June 2022;

Published online: 15 July 2022

References

1. Yamamoto, Y. et al. Direct observation of ferromagnetic spin polarization in gold nanoparticles. *Phys. Rev. Lett.* **93**, 116801 (2004).
2. Al Ma'Mari, F. et al. Beating the Stoner criterion using molecular interfaces. *Nature* **524**, 69–73 (2015).
3. Blundell, S. J. & Pratt, F. L. Organic and molecular magnets. *J. Phys.: Cond. Matter* **16**, R771 (2004).
4. Papaefthymiou, G. C. Nanoparticle magnetism. *Nano Today* **4**, 438–447 (2009).
5. Burch, K. S., Mandrus, D. & Park, J. G. Magnetism in two-dimensional van der Waals materials. *Nature* **563**, 47–52 (2018).
6. Choi, D. J. et al. Colloquium: Atomic spin chains on surfaces. *Rev. Mod. Phys.* **91**, 041001 (2019).
7. Coronado, E. Molecular magnetism: from chemical design to spin control in molecules, materials and devices. *Nat. Rev. Mater.* **5**, 87–104 (2020).
8. Marrows, C. H. Artificially Engineered Magnetic Materials. Handbook of Magnetism and Magnetic Materials, Springer, 1–34 (2020).
9. Lee, E. W. Magnetostriction and magnetomechanical effects. *Rep. Prog. Phys.* **18**, 184–229 (1955).
10. Pettifer, R. F., Mathon, O., Pascarelli, S., Cooke, M. D. & Gibbs, M. R. Measurement of femtometre-scale atomic displacements by X-ray absorption spectroscopy. *Nature* **435**, 78–81 (2005).
11. Ruffoni, M. P. et al. Direct measurement of intrinsic atomic scale magnetostriction. *Phys. Rev. Lett.* **101**, 147202 (2008).
12. Borovik-Romanov, A. S. Piezomagnetism in the antiferromagnetic fluorides of cobalt and manganese. *Sov. Phys. JETP* **11**, 786–793 (1960).
13. Lage, E. et al. Exchange biasing of magnetoelectric composites. *Nat. Mater.* **11**, 523–529 (2012).
14. Jaime, M. et al. Piezomagnetism and magnetoelastic memory in uranium dioxide. *Nat. Commun.* **8**, 1–7 (2017).
15. Claeysen, F., Lhermet, N., Le Letty, R. & Bouchilloux, P. Actuators, transducers and motors based on giant magnetostrictive materials. *J. Alloy. Compd.* **258**, 61–73 (1997).
16. Wang, Y., Hu, J., Lin, Y. & Nan, C. W. Multiferroic magnetoelectric composite nanostructures. *NPG Asia Mater.* **2**, 61–68 (2010).
17. Narita, F. & Fox, M. A review on piezoelectric, magnetostrictive, and magnetoelectric materials and device technologies for energy harvesting applications. *Adv. Eng. Mater.* **20**, 1700743 (2018).
18. Meisenheimer, P. B. et al. Engineering new limits to magnetostriction through metastability in iron-gallium alloys. *Nat. Commun.* **12**, 1–8 (2021).
19. Yanson, A. I., Rubio Bollinger, G., van den Brom, H. E., Agraït, N. & van Ruitenbeek, J. M. Formation and manipulation of a metallic wire of single gold atoms. *Nature* **395**, 783–785 (1998).
20. Ohnishi, H., Kondo, Y. & Takayanagi, K. Quantized conductance through individual rows of suspended gold atoms. *Nature* **395**, 780–783 (1998).
21. Smit, R. H. M., Untiedt, C., Yanson, A. I. & Van Ruitenbeek, J. M. Common origin for surface reconstruction and the formation of chains of metal atoms. *Phys. Rev. Lett.* **87**, 266102 (2001).
22. Smit, R. H. M., Untiedt, C., Rubio-Bollinger, G., Segers, R. C. & Van Ruitenbeek, J. M. Observation of a parity oscillation in the conductance of atomic wires. *Phys. Rev. Lett.* **91**, 076805 (2003).
23. Bettini, J. et al. Experimental realization of suspended atomic chains composed of different atomic species. *Nat. Nanotechnol.* **3**, 182–185 (2006).
24. Thijssen, W. H., Marjenburgh, D., Bremmer, R. H. & Van Ruitenbeek, J. M. Oxygen-enhanced atomic chain formation. *Phys. Rev. Lett.* **96**, 026806 (2006).
25. Csonka, S., Halbritter, A. & Mihály, G. Pulling gold nanowires with a hydrogen clamp: Strong interactions of hydrogen molecules with gold nanojunctions. *Phys. Rev. B* **73**, 075405 (2006).
26. Kizuka, T. Atomic configuration and mechanical and electrical properties of stable gold wires of single-atom width. *Phys. Rev. B* **77**, 155401 (2008).
27. Makk, P., Balogh, Z., Csonka, S. & Halbritter, A. Pulling platinum atomic chains by carbon monoxide molecules. *Nanoscale* **4**, 4739–4745 (2012).
28. Pauly, F. et al. Molecular dynamics study of the thermopower of Ag, Au, and Pt nanocontacts. *Phys. Rev. B* **84**, 195420 (2011).
29. Vardimon, R. et al. Probing the orbital origin of conductance oscillations in atomic chains. *Nano Lett.* **14**, 2988–2993 (2014).
30. Strigl, F., Espy, C., Bückle, M., Scheer, E. & Pietsch, T. Emerging magnetic order in platinum atomic contacts and chains. *Nat. Commun.* **6**, 1–9 (2015).

31. Vardimon, R., Klionsky, M. & Tal, O. Indication of complete spin filtering in atomic-scale nickel oxide. *Nano Lett.* **15**, 3894–3898 (2015).
32. Cui, L. et al. Quantized thermal transport in single-atom junctions. *Science* **355**, 1192–1195 (2017).
33. Klöckner, J. C., Matt, M., Nielaba, P., Pauly, F. & Cuevas, J. C. Thermal conductance of metallic atomic-size contacts: Phonon transport and Wiedemann-Franz law. *Phys. Rev. B* **96**, 205405 (2017).
34. Prestel, M. W., Ritter, M. F., Di Bernardo, A., Pietsch, T. & Scheer, E. Tuning the magnetic anisotropy energy of atomic wires. *Phys. Rev. B* **100**, 214439 (2019).
35. Ochiai, Y., Obi, T., Tsuruoka, Y. & Kizuka, T. Element mapping in single-atom-width platinum–iridium wires. *Nano Lett.* **20**, 2169–2174 (2020).
36. Delin, A. & Tosatti, E. Magnetic phenomena in 5 d transition metal nanowires. *Phys. Rev. B* **68**, 144434 (2003).
37. Fernández-Rossier, J., Jacob, D., Untiedt, C. & Palacios, J. J. Transport in magnetically ordered Pt nanocontacts. *Phys. Rev. B* **72**, 224418 (2005).
38. Smogunov, A., Dal Corso, A., Delin, A., Weht, R. & Tosatti, E. Colossal magnetic anisotropy of monatomic free and deposited platinum nanowires. *Nat. Nanotechnol.* **3**, 22–25 (2008).
39. Fernández-Seivane, L., García-Suárez, V. M. & Ferrer, J. Predictions for the formation of atomic chains in mechanically controllable break-junction experiments. *Phys. Rev. B* **75**, 075415 (2007).
40. Thiess, A., Mokrousov, Y., Heinze, S. & Blügel, S. Magnetically hindered chain formation in transition-metal break junctions. *Phys. Rev. Lett.* **103**, 217201 (2009).
41. Tung, J. C. & Guo, G. Y. Magnetic moment and magnetic anisotropy of linear and zigzag 4 d and 5 d transition metal nanowires: First-principles calculations. *Phys. Rev. B* **81**, 094422 (2010).
42. Thiess, A., Mokrousov, Y. & Heinze, S. Competing magnetic anisotropies in atomic-scale junctions. *Phys. Rev. B* **81**, 054433 (2010).
43. Crangle, J. & Scott, W. R. Dilute ferromagnetic alloys. *J. Appl. Phys.* **36**, 921–928 (1965).
44. Korenblit, I. Y. & Shender, E. F. Ferromagnetism of disordered systems. *Sov. Phys. Uspekhi* **21**, 832–851 (1978).
45. Cadeville, M. & Morán-López, J. L. Magnetism and spatial order in transition metal alloys: Experimental and theoretical aspects. *Phys. Rep.* **153**, 331–399 (1987).
46. Khajetoorians, A. A. et al. Tuning emergent magnetism in a Hund’s impurity. *Nat. Nanotech.* **10**, 958–964 (2015).
47. Shiota, T., Mares, A. I., Valkering, A. M. C., Oosterkamp, T. H., & Van Ruitenbeek, J. M. Mechanical properties of Pt monatomic chains. *Phys. Rev. B* **77**, 125411 (2008).
48. García-Suárez, V. M. et al. Conductance oscillations in zigzag platinum chains. *Phys. Rev. Lett.* **95**, 256804 (2005).
49. Da Silva, E. Z., da Silva, A. J. & Fazzio, A. How do gold nanowires break? *Phys. Rev. Lett.* **87**, 256102 (2001).
50. Rubio-Bollinger, G., Bahn, S. R., Agrait, N., Jacobsen, K. W. & Vieira, S. Mechanical properties and formation mechanisms of a wire of single gold atoms. *Phys. Rev. Lett.* **87**, 026101 (2001).
51. Manchon, A. & Belabbes, A. Spin-orbitronics at transition metal interfaces. *Solid State Phys.* **68**, 1–89 (2017).
52. Koseki, S., Matsunaga, N., Asada, T., Schmidt, M. W. & Gordon, M. S. Spin–Orbit coupling constants in atoms and ions of transition elements: comparison of effective core potentials, model core potentials, and all-electron methods. *J. Phys. Chem. A* **123**, 2325–2339 (2019).
53. Ishida, H. Embedded Green-function calculation of the conductance of oxygen-incorporated Au and Ag monatomic wires. *Phys. Rev. B* **75**, 205419 (2007).
54. Zhang, C., Barnett, R. N. & Landman, U. Bonding, conductance, and magnetization of oxygenated Au nanowires. *Phys. Rev. Lett.* **100**, 046801 (2008).
55. Strange, M., Thygesen, K. S., Sethna, J. P. & Jacobsen, K. W. Anomalous conductance oscillations and half-metallicity in atomic Ag–O chains. *Phys. Rev. Lett.* **101**, 096804 (2008).
56. Çakır, D. & Gülseren, O. Effect of impurities on the mechanical and electronic properties of Au, Ag, and Cu monatomic chain nanowires. *Phys. Rev. B* **84**, 085450 (2011).
57. Zheng, X., Xie, Y. Q., Ye, X. & Ke, S. H. Conductance and spin-filter effects of oxygen-incorporated Au, Cu, and Fe single-atom chains. *J. Appl. Phys.* **117**, 043902 (2015).
58. Koon, N. C., Williams, C. M. & Das, B. N. Giant magnetostriktion materials. *J. Magn. Mater.* **100**, 173–185 (1991).
59. Kaiser, U., Schwarz, A. & Wiesendanger, R. Magnetic exchange force microscopy with atomic resolution. *Nature* **446**, 522–525 (2007).
60. Pielmeier, F. & Giessibl, F. J. Spin resolution and evidence for superexchange on NiO(001) observed by force microscopy. *Phys. Rev. Lett.* **110**, 266101 (2013).
61. Lazo, C., Caciuc, V., Hölscher, H. & Heinze, S. Role of tip size, orientation, and structural relaxations in first-principles studies of magnetic exchange force microscopy and spin-polarized scanning tunneling microscopy. *Phys. Rev. B* **78**, 214416 (2008).
62. Granovskij, M., Schrön, A. & Bechstedt, F. Magnetic exchange force microscopy from first principles: application to the antiferromagnetic NiO(001) surface. *N. J. Phys.* **16**, 023020 (2014).
63. Peralta, J. E., Scuseria, G. E. & Frisch, M. J. Noncollinear magnetism in density functional calculations. *Phys. Rev. B* **75**, 125119 (2007).
64. Scalmani, G. & Frisch, M. J. A new approach to noncollinear spin density functional theory beyond the local density approximation. *J. Chem. Theory Comput.* **8**, 2193–2196 (2012).
65. Peralta, J. E., Hod, O. & Scuseria, G. E. Magnetization dynamics from time-dependent noncollinear spin density functional theory calculations. *J. Chem. Theory Comput.* **11**, 3661–3668 (2015).
66. Gaussian 16: Gaussian 16, Revision B.01, Frisch, M. J., et al. Gaussian, Inc., Wallingford, C. T. (2016).
67. Perdew, J. P., Ernzerhof, M. & Burke, K. Rationale for mixing exact exchange with density functional approximations. *J. Chem. Phys.* **105**, 9982–9985 (1996).
68. Ernzerhof, M. & Scuseria, G. E. Assessment of the Perdew–Burke–Ernzerhof exchange–correlation functional. *J. Chem. Phys.* **110**, 5029–5036 (1999).
69. Adamo, C. & Barone, V. Toward reliable density functional methods without adjustable parameters: The PBE0 Model. *J. Chem. Phys.* **110**, 6158–6170 (1999).
70. Figgien, D., Peterson, K. A., Dolg, M. & Stoll, H. Energy-consistent pseudopotentials and correlation consistent basis sets for the 5d elements Hf–Pt. *J. Chem. Phys.* **130**, 164108 (2009).
71. Tran, F., Blaha, P., Schwarz, K. & Novák, P. Hybrid exchange–correlation energy functionals for strongly correlated electrons: applications to transition-metal monoxides. *Phys. Rev. B* **74**, 155108 (2006).
72. Mandal, S., Haule, K., Rabe, K. M. & Vanderbilt, D. Systematic beyond-DFT study of binary transition metal oxides. *npj Comput. Mater.* **5**, 115 (2019).

Acknowledgements

O.T. appreciates the support of the Harold Perlman family, and acknowledges funding by a research grant from Dana and Yossie Hollander, the Israel Science Foundation (Grant No. 1089/15), the Minerva Foundation (Grant No. 120865), the Ministry of Science and Technology of Israel (Grant No. 3–16244), and the European Research Council, Horizon 2020 (Grant No. 864008). J.E.P. acknowledges support from the Office of Basic Energy Sciences, US Department of Energy (Grant No. DE-SC0005027). O.H. is grateful for the generous financial support of the Heineman Chair in Physical Chemistry, the Israel Science Foundation (Grant No. 1740/13), The Ministry of Science and Technology of Israel (Grant No. 3–16244), and the Center for Nanoscience and Nanotechnology of Tel-Aviv University. A.O. gratefully acknowledges the support of the Adams Fellowship Program of the Israel Academy of Sciences and Humanities. DFT calculations were done at the Institute for Cyber-Enabled Research at Michigan State University.

Author contributions

The project was conceived by O.T. and S.C. The experiments were designed by S.C., G.D. and O.T. and performed by S.C. and G.D., under the supervision of O.T. Experimental data analysis was done by S.C., G.D. and A.V., under the supervision of O.T. The minimal model was conceived by J.E.P. and O.H., and developed by J.E.P. The DFT calculations were performed and analyzed by J.E.P., A.O., and O.H. The manuscript was written by O.T., O.H. and J.E.P. All authors contributed to the final versions of the manuscript.

Competing interests

The authors declare no competing interests.

Additional information

Supplementary information The online version contains supplementary material available at <https://doi.org/10.1038/s41467-022-31456-4>.

Correspondence and requests for materials should be addressed to Oren Tal.

Peer review information *Nature Communications* thanks the anonymous reviewer(s) for their contribution to the peer review of this work.

Reprints and permission information is available at <http://www.nature.com/reprints>

Publisher’s note Springer Nature remains neutral with regard to jurisdictional claims in published maps and institutional affiliations.



Open Access This article is licensed under a Creative Commons Attribution 4.0 International License, which permits use, sharing, adaptation, distribution and reproduction in any medium or format, as long as you give appropriate credit to the original author(s) and the source, provide a link to the Creative Commons license, and indicate if changes were made. The images or other third party material in this article are included in the article's Creative Commons license, unless indicated otherwise in a credit line to the material. If material is not included in the article's Creative Commons license and your intended use is not permitted by statutory regulation or exceeds the permitted use, you will need to obtain permission directly from the copyright holder. To view a copy of this license, visit <http://creativecommons.org/licenses/by/4.0/>.

© The Author(s) 2022

Supplementary Information

Magnetic control over the fundamental structure of atomic wires

Sudipto Chakrabarti¹, Ayelet Vilan¹, Gai Deutch¹, Annabelle Oz², Oded Hod², Juan E. Peralta³ & Oren Tal¹

¹ Department of Chemical and Biological Physics, Weizmann Institute of Science, Rehovot 7610001, Israel

² School of Chemistry and the Sackler Center for Computational Molecular and Materials Science, Tel Aviv University, Tel Aviv 6997801, Israel

³ Department of Physics, Central Michigan University, Mt. Pleasant, Michigan 48859, United States

The supplementary information consists of 13 sections, as listed below:

Supplementary section 1: Conductance as a function of magnetic fields in Pt atomic wires

Supplementary section 2: Length calibration

Supplementary section 3: Applied voltage effect on the magneto-structural response of Pt wires

Supplementary section 4: Magneto-structural measurements in Au atomic wires

Supplementary section 5: d_{90} and its response to magnetic field

Supplementary section 6: Comparison between different wire length evaluations

Supplementary section 7: magnetic field effect on the number of atoms in Pt wires

Supplementary section 8: Magnetic field effect on the peak sharpness in the length histograms of Pt atomic wires

Supplementary section 9: First-principles calculations

Supplementary section 10: Description of the model

Supplementary section 11: Model sensitivity with respect to input parameters

Supplementary section 12: Temperature dependent measurements

Supplementary section 13: Absence of hysteresis

Supplementary section 1: Conductance as a function of magnetic fields in Pt atomic wires

Most probable conductance analysis:

We measure the conductance G ($G=1/R$, where R is the resistance) as a function of magnetic field by fixing the field and collecting 10,000 conductance traces as a function of inter-electrode displacement (see Fig. 1b of the main text). These traces are used to construct conductance histograms at different magnetic fields as seen in Figs. S1a-h. The observed peak at about $1.6 G_0$ in these histograms provides the most probable conductance of the Pt atomic wires. The conductance above the $1.6 G_0$ peak is the outcome of contacts with more than one atom in their cross section that are formed before wire elongation, and the tail at low conductance stems from tunneling conductance that follows wire rupture. The figures show a sequence of conductance histograms taken one after the other at different magnetic field magnitudes, either perpendicular or parallel to the junction's axis. We do not observe any indications for a systematic shift in the conductance peak at $\sim 1.6 G_0$ as a function of magnetic field. Figs. S1i,j show the average value of the conductance peak maximum as a function of perpendicular (i) and parallel (j) magnetic fields for several measurement sets, similar to the two sets presented in Figs. S1a-h. Each data point is an average based on at least 8 different conductance histograms collected at a given magnetic field but in different experimental sessions. As exemplified in Figs. S1i,j, in the limit of the experimental error, we do not find any magnetic-induced variations in the conductance of Pt atomic wires.

We note that our analysis is insensitive to possible magnetoresistance variations that might exist in atypical and infrequently-formed structures of Pt atomic wires or to finite magnetoresistance with an arbitrary sign for different junction realizations, since we average-out their possible contributions. Furthermore, we cannot detect very small magnetic-induced conductance variations of the order of a few percent, since they are in the range of the minor differences in the peak locations sometimes detected in different conductance histograms regardless of the presence or absence of an external magnetic field. Such variations can possibly stem from changes in the atomic structure of the electrodes. These characteristics of ensemble-based analysis may explain the discrepancy between our transport measurements and the one reported in Ref. 1 (Ref. 14 in the main text).

The approach that we use in our analysis has an important advantage. In magnetoresistance measurements, variations in resistance (or conductance) can be an outcome of magnetostriction effects rather than pure magnetoresistance of electronic origin. Such undesirable magnetostrictive effects can take place when the inter-electrode distance is kept constant after an atomic wire is formed and then a magnetic field is swept. In this case, conductance variations as a function of magnetic field can stem from magnetic-induced structural variations, such as: (i) extrinsic magnetostriction-induced changes in the dimensions of the sample or sample-holder that lead to changes in the interelectrode distance; (ii) intrinsic magnetostriction, where the interelectrode distance remains intact but possible changes in the wire length and tension in response to magnetic field variations may lead to

conductance changes. In our measurements, we avoid these unwanted effects by performing repeated conductance measurements during wire elongation under a fixed magnetic field. As mentioned in the main text, minor conductance variations due to the reported magnetic effect on the interatomic distance are expected to be smaller than the uncertainty range of the presented ensemble analysis in Figs. S1i,j.

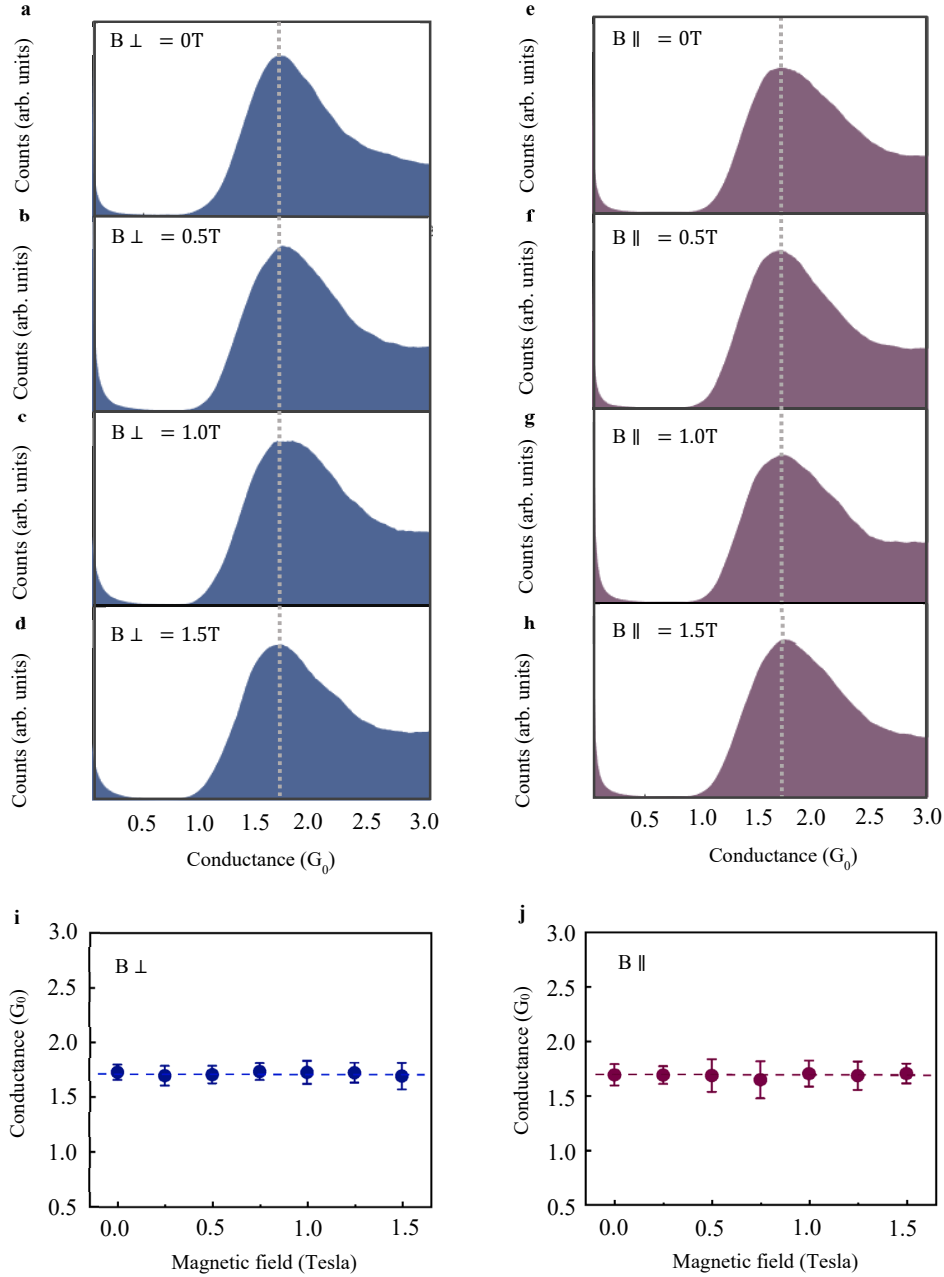


Fig. S1 Conductance as a function of applied magnetic fields during the formation of Pt atomic wires. a-d, Conductance histograms collected at different magnetic fields perpendicular to the junction’s axis. **e-h,** Similar to a-d but for a parallel magnetic field. **i,** Conductance at the peak maximum as a function of magnetic field perpendicular to the junction’s axis. **j,** Similar to i but for a parallel magnetic field. In i,j each data point is an average of the peak value, based on at least 8 different conductance histograms taken in different experimental sessions. Each such histogram is composed of 10,000 conductance traces, measured under a bias voltage of 20 mV. The error bars are the standard deviation of peaks’ maxima. No magnetoresistance is detected within the measurement uncertainty. Figs. S1i,j appear in the main text as Insets in Fig. 1g,h.

Conductance oscillations during wire elongation:

As mentioned above and in the main text, we do not observe variations in the most probable conductance larger than several percent. However, we find clear indications for the effect of applied magnetic fields on electronic transport when focusing on conductance as a function of elongation. Figure S2, presents the average conductance measured during wire elongation under parallel (a), zero (b), and perpendicular (c) applied magnetic fields. Clear conductance oscillations are seen riding on a decaying conductance baseline. These oscillations are ascribed to variations in the local orbital structure during the elongation process of Pt atomic wires^{2,3}. Specifically, a relaxed wire has a zigzag structure, however, when the wire is stretched it becomes linear. This results in an enhanced orbital hybridization and higher density of states at the Fermi energy, translated to conductance increase. Further stretching results in either rupture or the insertion of another atom into the wire, and partial relaxation of the wire back to the less-conducting zigzag configuration. Therefore, during wire elongation the conductance oscillates (Fig. S2) and the magnitude of these oscillations probes the extent of orbital overlap at the Fermi level³.

Focusing on the influence of parallel and perpendicular magnetic fields on the amplitude of the conductance oscillations (Fig. S2), we find that a perpendicular magnetic field enhances the oscillations and a parallel field suppresses them. These findings provide another indications that magnetic fields affect the orbital structure, and specifically a perpendicular (parallel) magnetic field enhances (suppresses) orbital overlap at the Fermi level. Transport measurements probe the states located in a window around the Fermi energy (about 20 meV in our case). In contrast, the magneto-structural response probes variations in the orbitals that are involved in the interatomic bonds that are not limited to the vicinity of the Fermi level. Thus, the two types of analysis complement each other. We note that the magnetic induced changes in the amplitude of the oscillations is clear, though it is limited to a few percent and therefore not seen in the most probable conductance analysis.

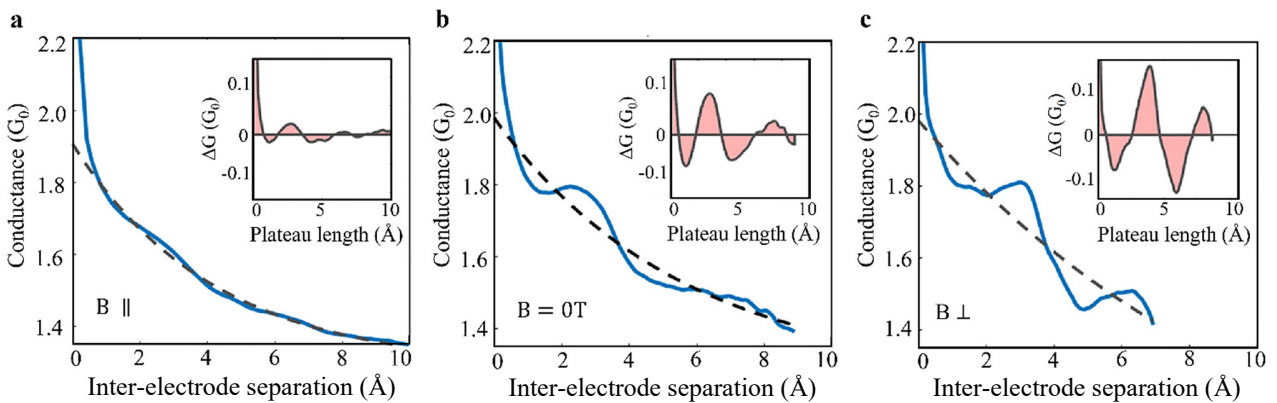


Fig. S2 Magnetic field effect on the average conductance traces of Pt atomic wires. a-c, Average conductance (blue) as a function of inter-electrode separation under a parallel magnetic field of 1.5 T (a), no applied magnetic field (b), a perpendicular magnetic field of 1.5 T (c) for applied bias voltage of 20 mV. The dashed black line is an exponential fit. Insets, difference between the average traces and the exponential fit. The observed conductance oscillations are enhanced (suppressed) when a perpendicular (parallel) magnetic field is applied. The data of each panel is based on 10,000 conductance traces taken at an applied bias voltage of 20 mV.

Supplementary section 2: Length calibration

The relative displacement of the electrodes in our break junction setup is proportional to the voltage applied on the piezo element (piezo voltage). We find the calibration constant between the piezo voltage and the inter-electrodes displacement based on the exponential decay of the conductance with distance in the tunneling regime (Fig. S3) as described in more details in Ref. 4 and its supplementary materials. Specifically, we collect histograms of the calibration constant based on thousands of traces of conductance as a function of piezo voltage to obtain a statistically reliable calibration (Fig. S3, Inset). The measured average inter-peak distance at zero applied magnetic field, which is determined based on the found calibration constant is in agreement with the value of $2.3 \pm 0.2 \text{ \AA}$ that appears in the literature^{5,6}. We note in passing that in our work the key information is the magnetic-field-induced variations in the inter-peak distance and the d_{90} rather than their absolute values.

The calibration factor may, in principle, vary in response to different magnetic fields. This is due to magnetostriction response that can affect the dimensions of the sample and sample-related components (the phosphor-bronze sample substrate, sample holder, etc.). Therefore, the relevant setup components and the sample itself are composed of materials with negligible magnetostriction. We verify that magnetic fields do not affect the calibration factor by repeating our measurements with gold (Au) atomic wires, which are not expected to exhibit any magnetic response in the relevant magnetic field range. As can be seen in Supplementary section 3, we did not detect any variations in the interatomic distances and d_{90} in response to magnetic fields for the case of Au atomic wires. This indicates that the calibration factor in our experimental setup is not affected by magnetic fields, for any practical purpose.

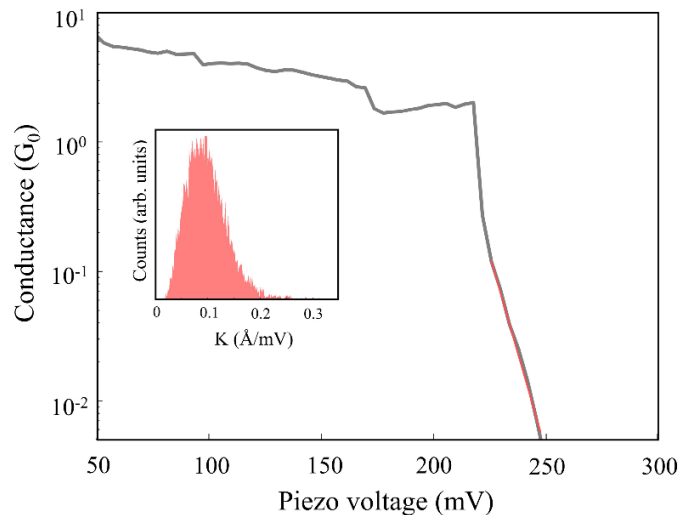


Fig. S3 Length calibration by conductance dependence on piezo voltage. Conductance as a function of piezo voltage measured during the increase of the distance between the electrode apices. The red line is an exponential fit to the tunneling conductance dependence on inter-electrode distance. **Inset:** histogram of the constant K relating the inter-electrode distance and the applied piezo voltage.

Supplementary section 3: Applied voltage effect on the magneto-structural response of Pt wires

Figures S4 and S5 show no apparent effect of applied bias voltage on the reported magneto-structural response, when increasing the bias from 20 mV to 100 mV and 180 mV. This analysis is limited to 180 mV, since we typically observe clear shortening of atomic wires due to Joule heating at above 200 mV or higher bias voltages.

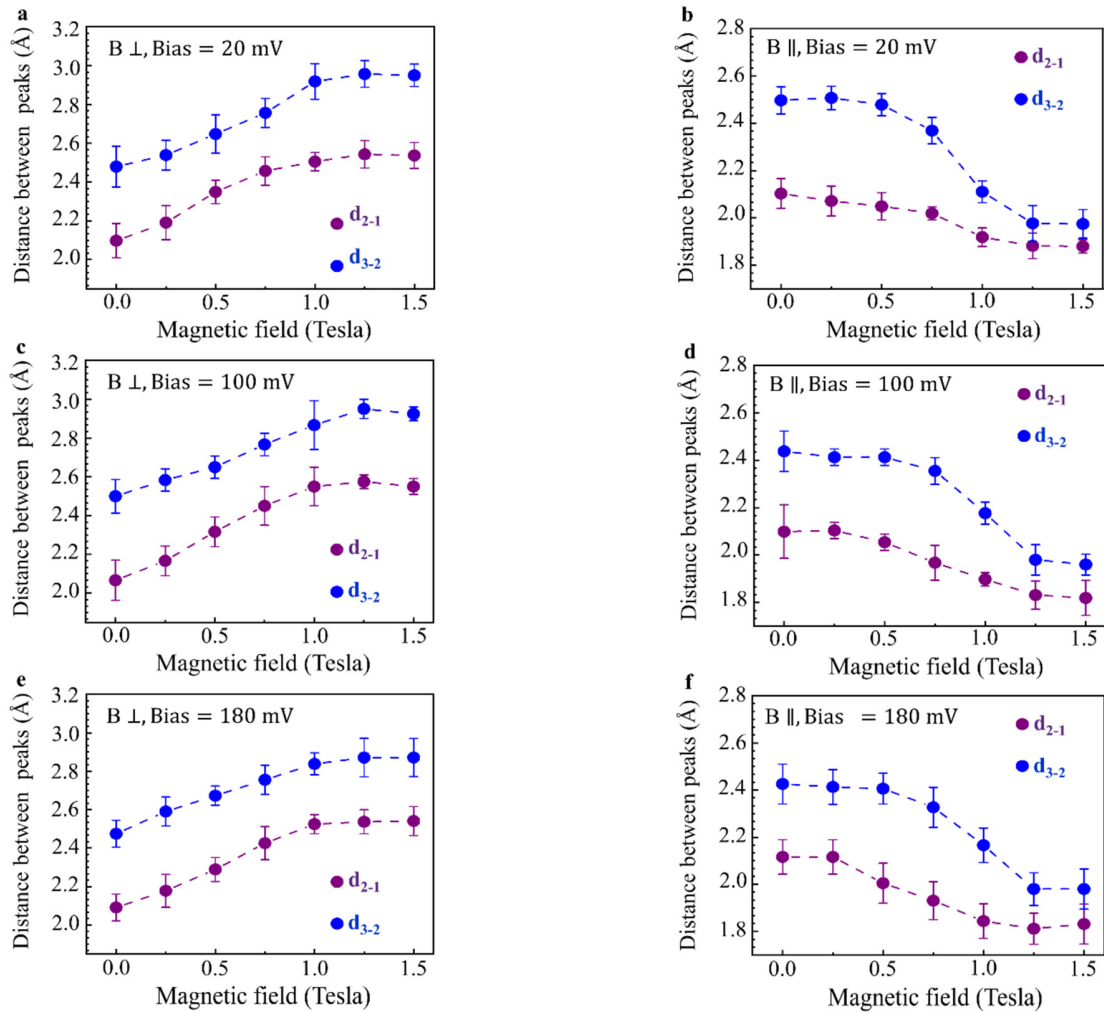


Fig. S4 Magnetic field effect on interatomic distance in Pt atomic wires. **a,b**, Inter-peak distance as a function of perpendicular (a) and parallel (b) magnetic fields for an applied bias voltage of 20 mV. d_{2-1} and d_{3-2} are the inter-peak distances as defined in Fig. 2 of the main text, which provide an indication for the average interatomic distance in the elongated wires. **c,d**, Similar to a,b, but with an applied bias voltage of 100 mV. **e,f**, Similar to a,b, but with an applied bias voltage of 180 mV. No significant detectable dependence on bias voltage is found. Each data point was obtained from at least 8 length histograms that were collected during different experimental sessions. Each such length histogram is based on 10,000 conductance traces. The error bars provide the standard deviation of the averaged data.

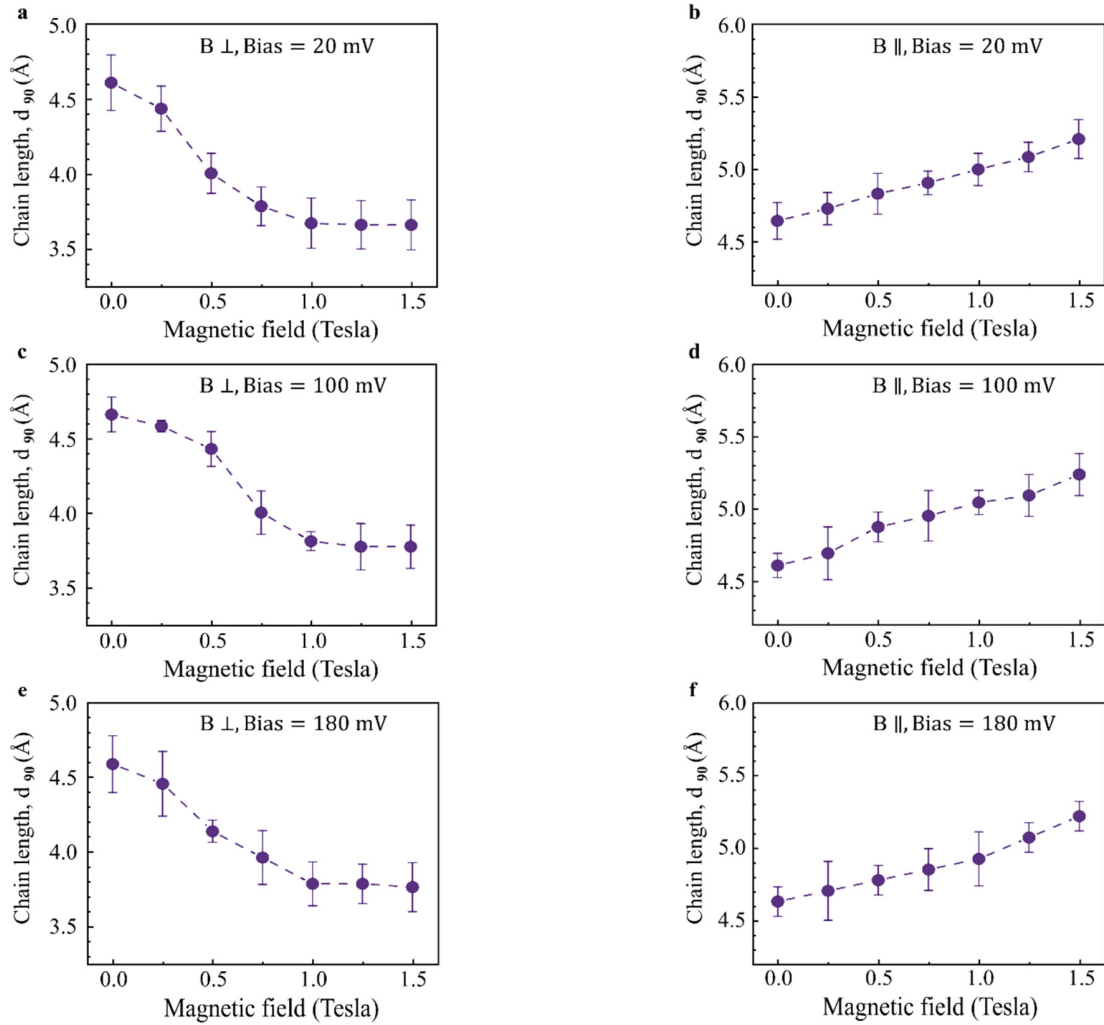


Fig. S5 Magnetic field effect on length of Pt atomic wires. **a,b**, d_{90} , a measure of the wire length as defined in the main text, as a function of perpendicular (a) and parallel (b) magnetic fields for an applied bias voltage of 20 mV. **c,d**, Similar to a,b, but with an applied bias voltage of 100 mV. **e,f**, Similar to a,b, but with an applied bias voltage of 180 mV. No significant detectable dependence on bias voltage is found. Each data point was obtained from at least 8 length histograms that were collected during different experimental sessions. Each such length histogram is based on 10,000 conductance traces. The error bars provide the standard deviation of the averaged data.

Supplementary section 4: Magneto-structural measurements in Au atomic wires

The magnetization and magnetic anisotropy of Au atomic wires are expected to be negligible⁷. Therefore, we repeat our entire experimental analysis with Au atomic wires as a control experiment. As can be seen in Fig. S6 and Fig. S7, the inter-peak distance and atomic wire length are not sensitive to parallel or perpendicular magnetic field in the range used in the main text for Pt wires. Interestingly, Fig. S8 shows that the peak width is not affected by a parallel magnetic field, but it increases for a perpendicular magnetic field. This indicates a different magneto-structural effect in comparison to the case of Pt atomic wires. This effect will be reported elsewhere.

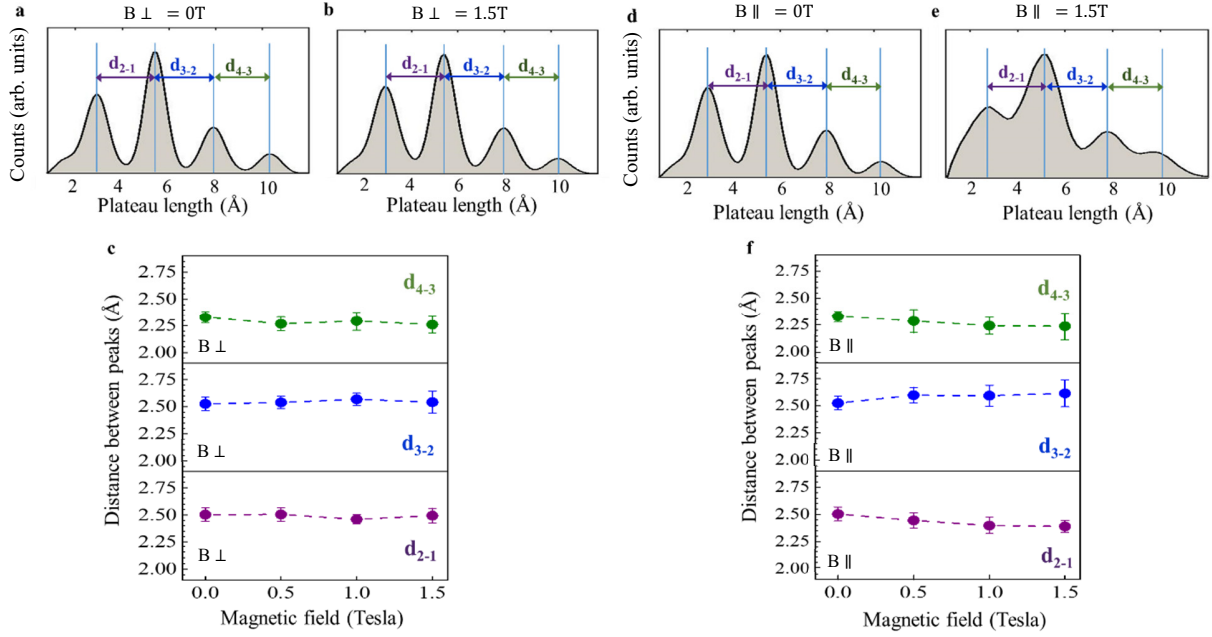


Fig. S6 Inter peak distance in Au length histograms as a function of magnetic field. **a,b**, Length histograms formed at zero applied magnetic field and at a magnetic field of 1.5 T (Tesla) perpendicular to the junction's axis, as defined in Fig. 1a. d_{2-1} , d_{3-2} and d_{4-3} are the inter-peak distances, which are good measures for the average interatomic distance in the elongated wires. **c**, Inter-peak distance as a function of a perpendicular magnetic field. No change in the inter-peak distance is observed within the experimental uncertainty (standard deviation). **d,e**, Similar to a,b but the magnetic field applied parallel to the junction's axis, as defined in Fig. 1a of the main text. **f**, Similar to c but with a parallel magnetic field. Here, as well, no change in the inter-peak distance is observed within the experimental uncertainty. All length histograms are based on 5,000 conductance traces, measured under a bias voltage of 20 mV.

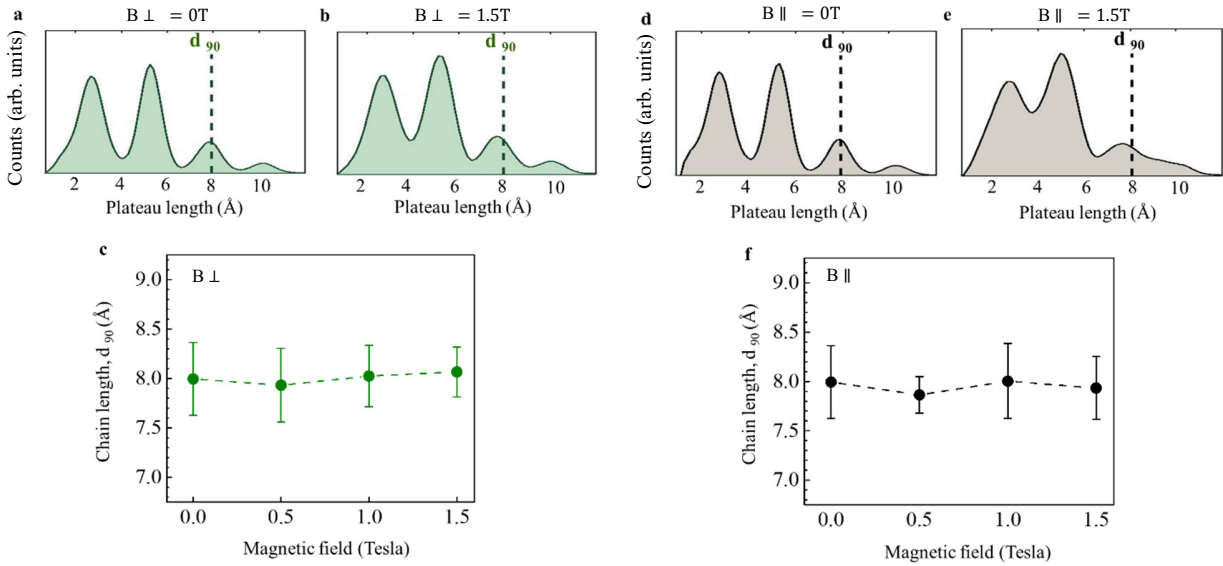


Fig. S7: Wire length for Au atomic wires as a function of magnetic field. **a,b**, Length histograms formed at zero magnetic field and at a magnetic field of 1.5 T applied perpendicular to the junction's axis, as defined in Fig. 1a of the main text. The dashed line represents the location of d_{90} , which is a measure of the wire length as explained in the main text. **c**, d_{90} as a function of a perpendicular magnetic field to the junction's axis. **d,e**, Similar to a,b but with a parallel magnetic field. **f** d_{90} as a function of a parallel magnetic field. Panels c and f compile results of at least 5 measurements. All length histograms are based on 5,000 conductance traces, measured under a bias voltage of 20 mV. The error bars represent the corresponding standard deviation. No change in d_{90} is observed as a function of magnetic field for Au atomic wires within the experimental uncertainty.

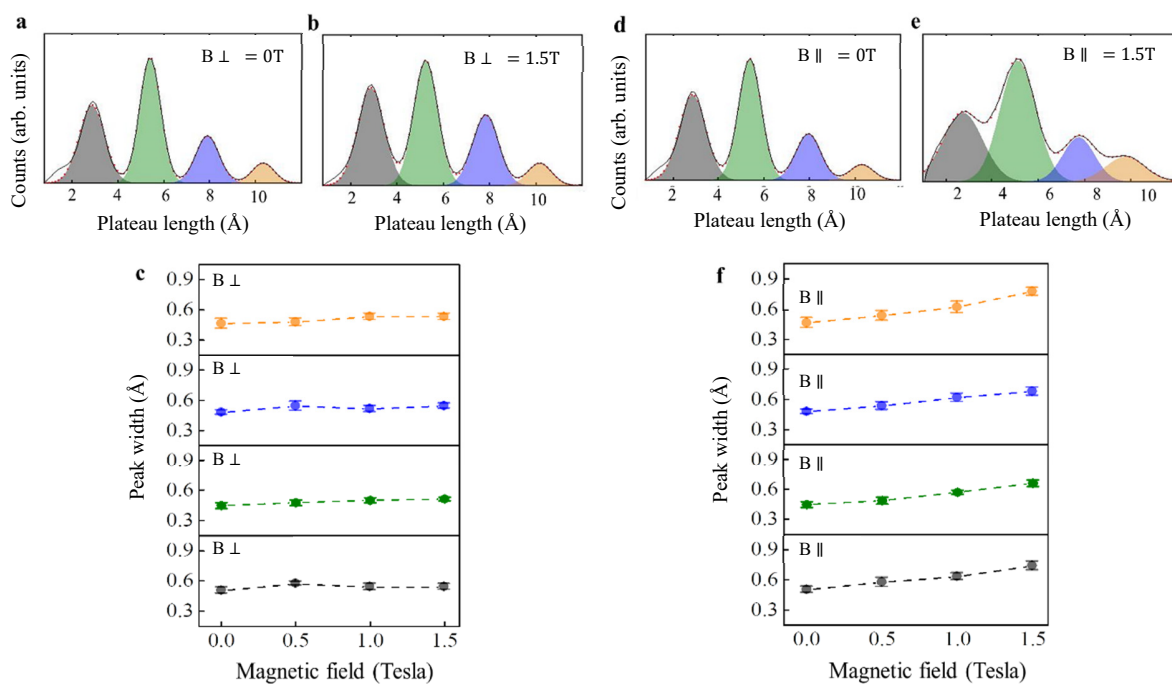


Fig. S8 Peak width for Au atomic wires as function of magnetic field. **a,b,** Show length histograms for atomic wires in the absence of magnetic field and under a field of 1.5 T applied perpendicular to the junction's axis, respectively. The peaks are fitted by Gaussian functions (red dots). **c,** Peak widths (obtained from the Gaussian fitting) as a function of magnetic field strength applied perpendicular to the junction's axis. **d,e,** Similar to a,b, but for a parallel magnetic field. **f,** Similar to c, but for a parallel magnetic field. Panels c,f compile results of at least 5 measurements. The error bars represent the corresponding standard deviation. All length histograms are based on 5,000 conductance traces, measured under a bias voltage of 20 mV.

Supplementary section 5: d_{90} and its response to magnetic field

As mentioned above (and in the main text), to evaluate the length of the Pt atomic wires we have defined the parameter, d_{90} , such that 90% of the formed wires are shorter than its value. This parameter is more reliable than the evaluation of the maximal wire length, which is determined by a limited number of long wires and thus is highly sensitive to variations between different experiments. Fig. S9 presents the location of d_{90} with respect to the corresponding length histograms and the influence of perpendicular and parallel magnetic fields on this parameter. d_{90} reduces in response to a magnetic field applied perpendicular to the junction's axis, whereas it increases when a magnetic field is applied parallel to the junction.

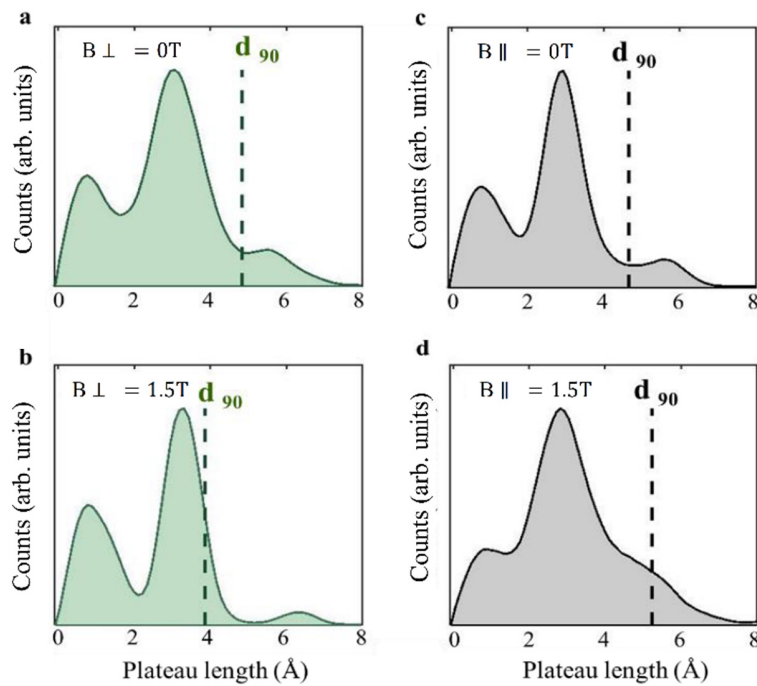


Fig. S9 The location of d_{90} within the Pt length histogram and its response to magnetic field. **a,b**, Length histograms constructed from 10,000 conductance traces in the absence of magnetic field (a) and in the presence of a magnetic field of 1.5 T applied perpendicular to the junction's axis (b). **c,d**, Similar to a,b, but for a parallel magnetic field. The dashed line represents the location of d_{90} . The measurements were performed using a bias voltage of 20 mV.

Supplementary section 6: Comparison between different wire length evaluations

To verify that the observed trends in d_{90} in response to magnetic field direction and strength in Fig. 2 of the main text is not sensitive to the exact definition of the wire length parameter, we examine the magnetic field dependence of d_{70} , and d_{95} . The definition of d_x is analogous to the one of d_{90} , as discussed in Supplementary Section 4 above, with $x\%$ of the atomic wires being shorter than d_x . Fig. S10 reveals that the magnitude of the magnetic-induced shifts is different for different d_x , but the shift trends are identical. Namely, the qualitative

behavior is preserved. Similar trends can be seen in Fig. S11 that presents the magnetic-field dependence of the average length of the 10 longest wires.

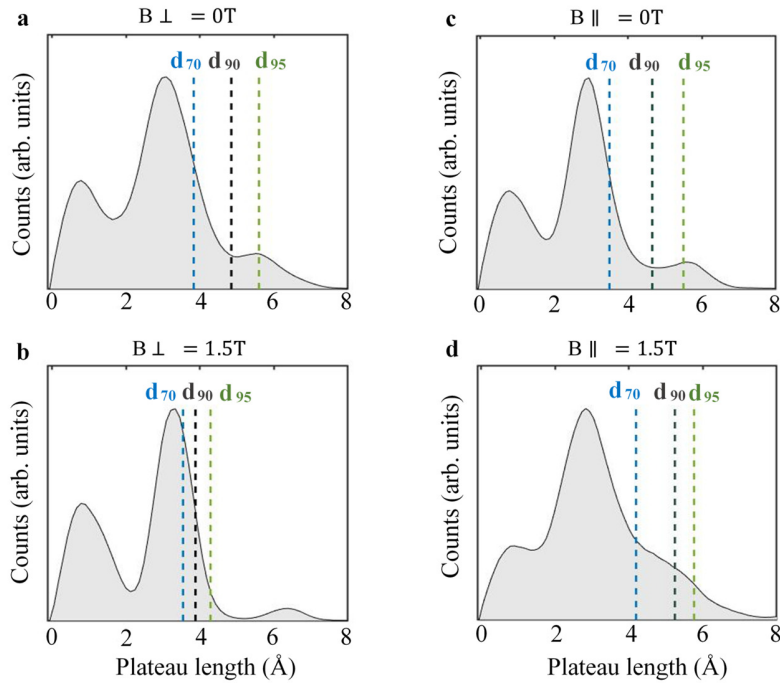


Fig. S10 d_x response to magnetic fields. **a,b**, Length histograms constructed from 10,000 conductance traces in the absence of a magnetic field (a) and in the presence of a magnetic field of 1.5 T applied perpendicular to the junction’s axis (b). Vertical dashed lines represent the location of d_x , $x=70\%$ (light blue), 90% (black), and 95% (green). **c,d**, Similar to a,b, but for a parallel magnetic field. The measurements were performed using a bias voltage of 20 mV.

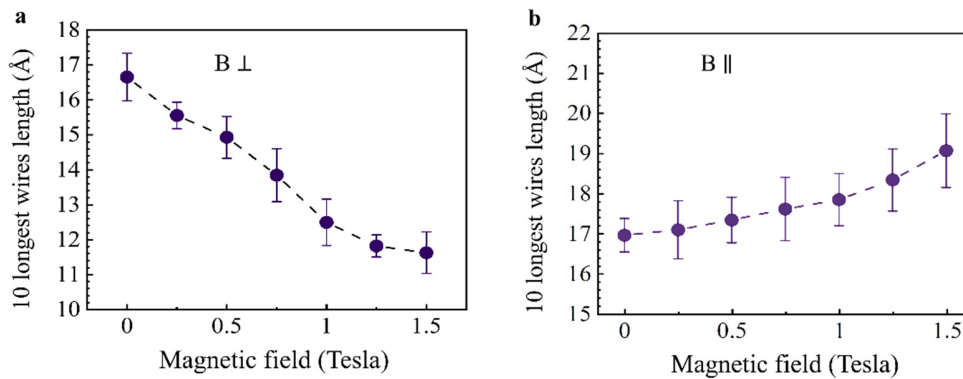


Fig. S11 Longest wires response to magnetic field. Averaged length of the ten longest atomic wire as a function of magnetic field applied perpendicular (a) and parallel (b) to the junction’s axis. For each magnetic field, 5 different sets of 10,000 conductance traces each were measured, then the average length of the 10 longest plateaus at $\sim 1.6 G_0$ were calculated for each set. The average and standard deviation of these values for the 5 sets are presented.

Supplementary section 7: magnetic field effect on the number of atoms in Pt wires

Figs. S12a,b show an estimation of the average number of atoms in Pt atomic wires as a function of magnetic field. This information is obtained by dividing the wire length by the interatomic distance. Specifically, the wire length is given by d_{90} and the interatomic distance is given by the average inter peak distance $((d_{3-2} + d_{2-1})/2)$ at each magnetic field. Based on Figs. S12a,b, a parallel magnetic field increases the average number of atoms in the wires by 0.7 ± 0.1 atoms and a perpendicular magnetic field decreases it by 0.7 ± 0.1 atoms. We repeat this analysis for the average length of the ten longest atomic wires to get a similar, though pronounced, behavior as seen in Figs. S12c,d. Here, the length increases by 2.3 ± 0.5 atoms or decreases by 3.1 ± 0.4 atoms for the same fields, indicating a higher sensitivity of the longest wires to magnetic fields. This is expected, considering that the wire's magnetization increases for longer wires⁸. This analysis estimates the magnetic field effect on the number of atoms added to or subtracted from the wires, and it does not provide an accurate estimation for the number of atoms in the wires that depends on the exact definition of where the wires begin/end.

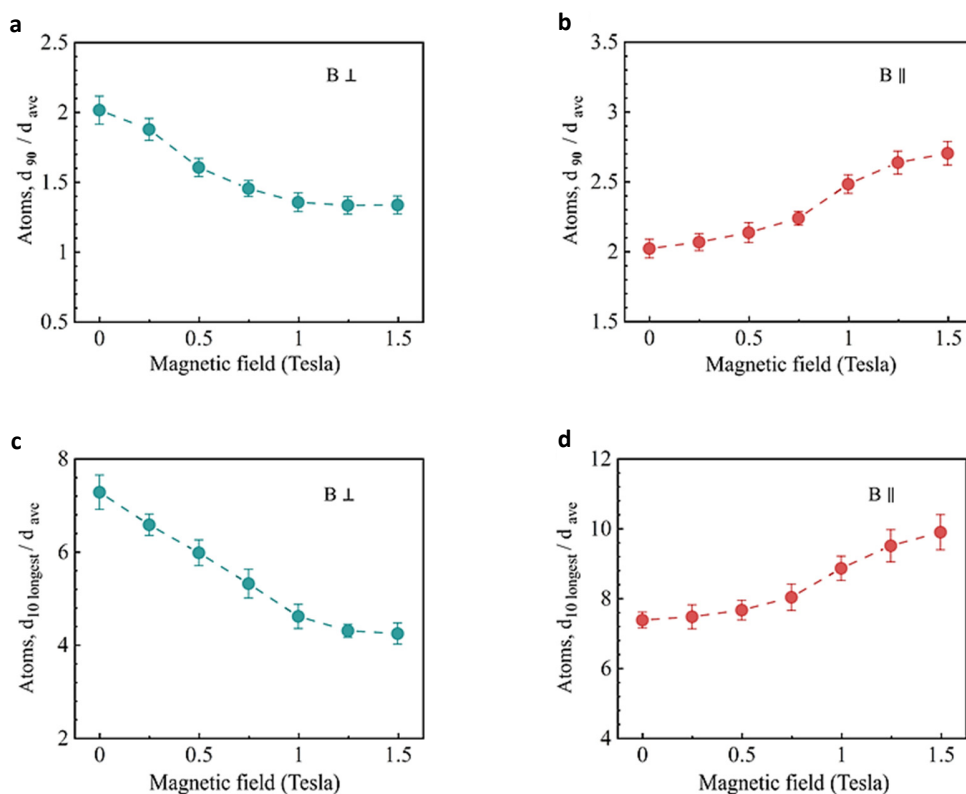


Fig. S12 Number of atoms in Pt atomic wires as a function of magnetic field. **a,b**, d_{90} divided by the interatomic distance given by the average inter peak distance ($d_{ave} = (d_{3-2} + d_{2-1})/2$), at the relevant magnetic field magnitude. The resulted number of atoms is plotted as a function of perpendicular (a) and parallel (b) magnetic fields. **c,d**, Average length of the longest 10 wires ($d_{10 \text{ longest}}$) divided by the average inter peak distance, at the relevant magnetic field magnitude. The resulted number of atoms is plotted as a function of perpendicular (c) and parallel (d) magnetic fields. The number of atoms decreases by 0.68 atoms for the d_{90} analysis (3.07 atoms for the 10 longest wires) when a perpendicular magnetic field is applied, and it increases by 0.69 atoms (2.25 atoms for the 10 longest wires) when a parallel field is applied.

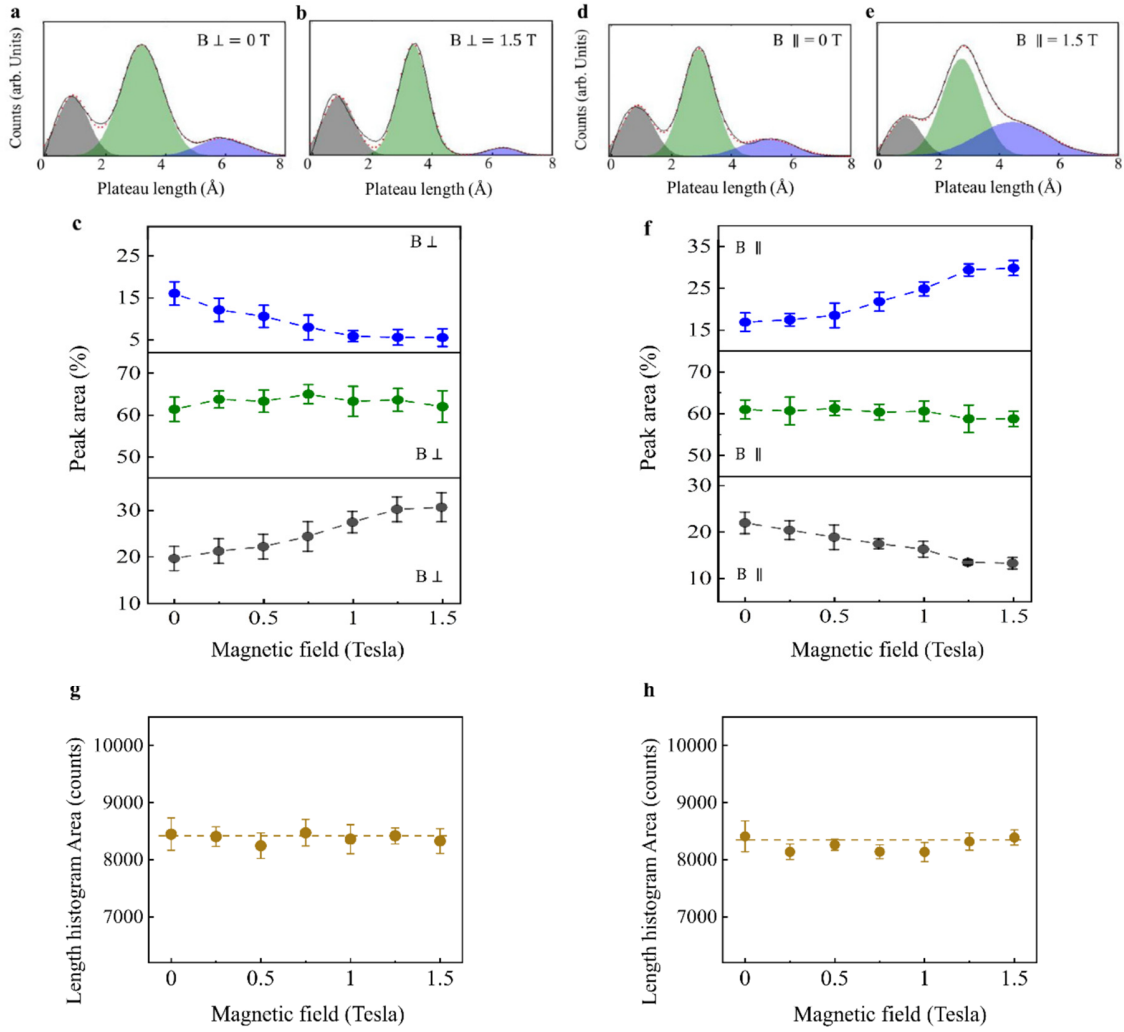


Fig. S13 Magnetic field effect on the peak area in the length histograms of Pt atomic wires. **a,b,d,e**, Length histograms (based on 10,000 conductance traces measured under a bias voltage of 20 mV) recorded at zero magnetic field (a,d), and at a field strength of 1.5 T applied perpendicular (b) or parallel (e) to the junction's axis. The peaks are fitted with Gaussian functions (red dots) and the sum of these fits appears in black. **c,f**, Areas of the fitted Gaussians as a function of the applied perpendicular (c) and parallel (f) magnetic field strength for the three peaks. The colors correspond to the peak colors appearing in a,b. Each data point provides the average area based on at least 8 length histograms taken at different experimental sessions under the same magnetic field. Error bars represent the corresponding standard deviation. **g,h**, Total areas of length histograms as a function of applied perpendicular (a) and parallel (b) magnetic fields. Each point represents the average area of 8 histograms (c,d) or 5 histograms (g,h). The error bars indicate the variance at each point.

Next, we focus on the relative weights of the peaks in the length histograms. Using Gaussian fittings, Figs. S13a-f present the relative area of each peak with respect to the total area of all peaks as a function of magnetic field. In response to the application of a parallel magnetic field, the area below the 3rd peak increases, while the area below the 1st peak decreases. The application of a perpendicular field leads to an opposite trend. Interestingly, the area below the 2nd peak is not very sensitive to magnetic fields, indicating that changes in the populations of the 1st and 3rd peaks are done on account of each other, while the population of 2nd peak is not significantly affected. The preservation of the 2nd peak can be understood in the following way. When a parallel field is applied, a larger

number of wires successfully survive rupture at the 1st peak and are being elongated to the 2nd peak. However, a similar number of wires successfully survive rupture at the 2nd peak as well, and are being elongated to the 3rd peak. We note that when examining the total area below the length histogram (Fig. S13g,h), we find a negligible change that can be rationalized as an outcome of the mentioned balance: the pronounced elongation to the 3rd peak is compensated by the suppression of wires that are broken in the 1st peak.

Supplementary section 8: Magnetic field effect on the peak sharpness in the length histograms of Pt atomic wires

In different length histograms taken in the absence of a magnetic field, arbitrary changes in the sharpness of the peaks may take place. This is probably due to changes in the atomic arrangement of the electrode apices. To clearly present the effect of magnetic field on the sharpness (or width) of the peaks in the length histograms, in Fig. 3 of the main text as well as in Figs. S14-S15 (presenting an extended version of Fig. 3), we deliberately choose an initial length histogram with wide (sharp) features at $B = 0$ T and then apply a perpendicular (parallel) magnetic field to exemplify the full range of peak widths response to the magnetic field.

To demonstrate that this choice does not influence our conclusions, in Fig. S16 we start with length histograms of similar sharpness before applying a magnetic field either parallel or perpendicular to the junction's axis. Then, we quantitatively analyze the effect of the magnetic fields on the peak width by fitting Gaussian functions to the peaks and examining the magnetic field influence on the Gaussian widths (Figs. S16a,b,d,e). Figs. S16c,f present the response of the Gaussian width, where each data point is an average based on at least 8 histograms per magnetic field value. For a perpendicular magnetic field, a clear reduction in the peaks' width is seen for the second and third peaks, while there is no clear influence on the first peak. For a parallel magnetic field, an increase in the width of the third peak is observed. The minor increase in the width of the second peak is of the order of the measurement uncertainty and we do not detect any magnetic field influence on the first peak. Former density functional theory (DFT) calculations showed that the magnetic moment in Pt atomic wires increases as a function of their length⁸, probably up to saturation. Therefore, shorter atomic wires are expected to have lower or no magnetic moment, explaining the observed reduced sensitivity of such wires to the external magnetic field.

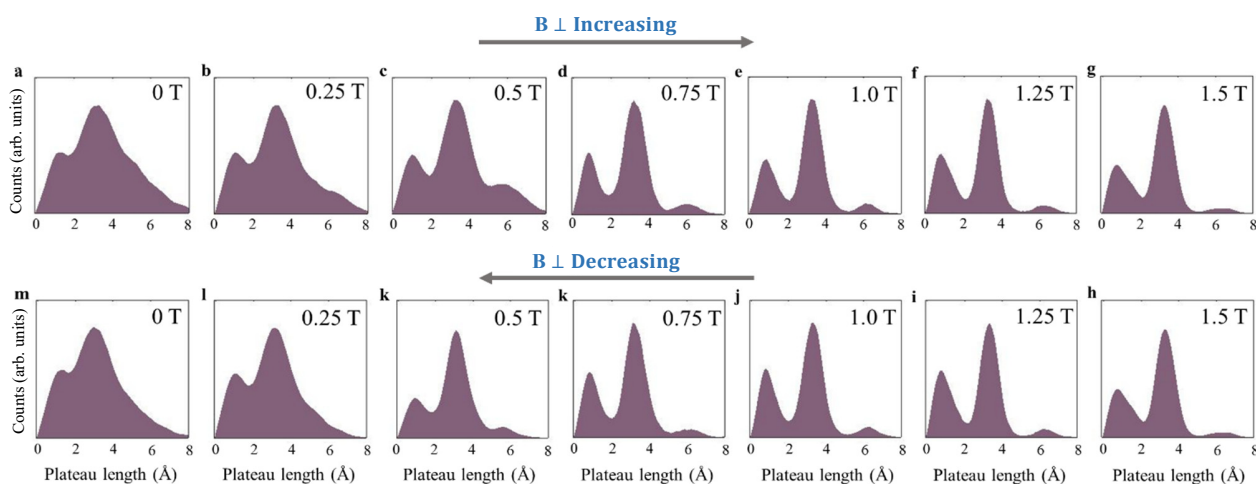


Fig. S14 The effect of perpendicular magnetic field on the peak sharpness in the length histograms of Pt atomic wires. Length histograms recorded sequentially as a function of increasing (a-g) and decreasing (m-h) magnetic field applied perpendicular to the junction's axis. The peaks' sharpness increases for higher magnetic field strengths. This response is inverted when the magnetic field is reduced. All length histograms are based on 10,000 conductance traces measured under a bias voltage of 20 mV.

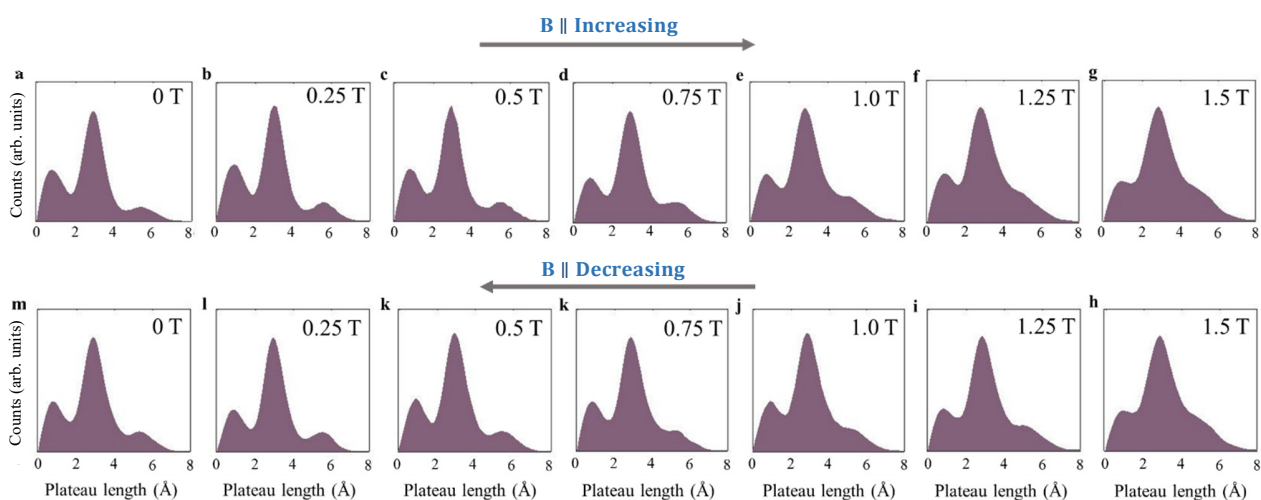


Fig. S15 The effect of parallel magnetic field on the peak sharpness in the length histograms of Pt atomic wires. Length histograms recorded sequentially as a function of increasing (a-g) and decreasing (m-h) magnetic field applied perpendicular to the junction axis. The peaks' sharpness decreases for higher magnetic field strengths. This response is inverted when the magnetic field is reduced. All length histograms are based on 10,000 conductance traces, measured under a bias voltage of 20 mV.

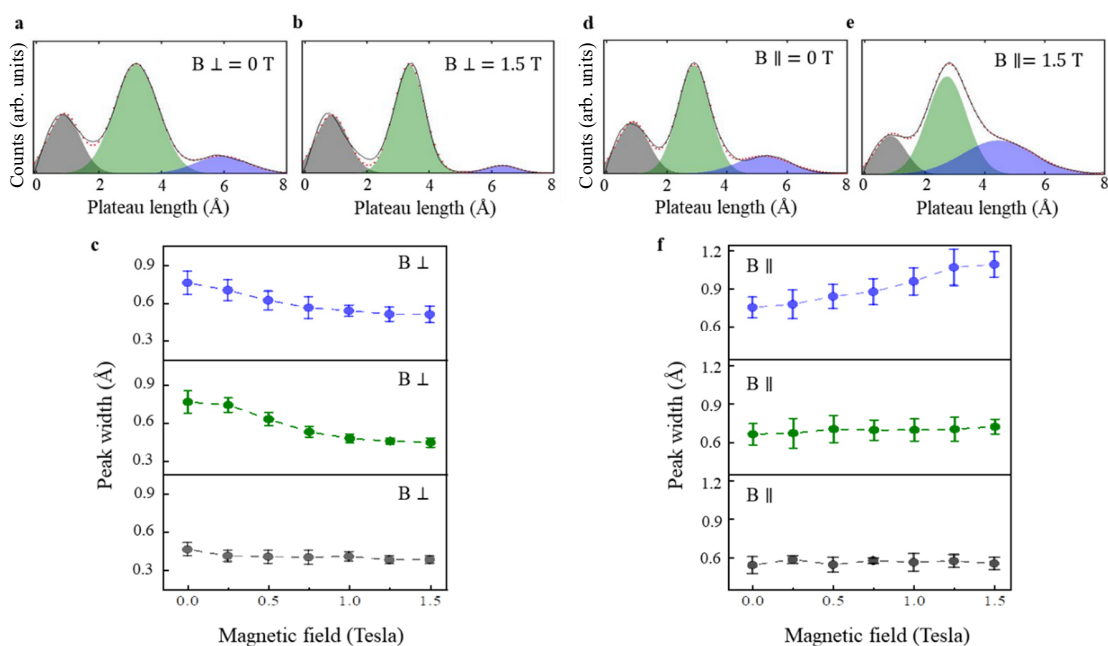


Fig. S16 Magnetic field effect on the peak width in the length histograms of Pt atomic wires. **a,b**, Length histograms (based on 10,000 conductance traces measured under a bias voltage of 20 mV) recorded at zero magnetic field and at a field strength of 1.5 T applied perpendicular to the junction's axis, respectively. The peaks are fitted with Gaussian functions (red dots) and the sum of these fits appears in black. **c**, Widths of the fitted Gaussians as a function of the applied perpendicular magnetic field strength for the three peaks. The colors correspond to the peak colors appearing in a,b. Each data point provides the average width based on at least 8 length histograms taken at different experimental sessions under the same magnetic field. Error bars represent the corresponding standard deviation. **d,e**, Similar to a,b, but for a parallel magnetic field. **f**, Similar to c, but for a parallel magnetic field.

Supplementary section 9: First-principles calculations

Zigzag to linear atomic wire transition

Pt atomic wires are known to have a zigzag structure near equilibrium^{2,3,7}. Nevertheless, upon stretching, the wires become linear^{2,3,7}. To obtain a qualitative description of the stretching process from compact zigzag wire configurations up to the breaking point, we performed DFT calculations (see technical details below) on junction models consisting of 1- and 2- Pt atoms bridging two Pt₁₄ square pyramidal structures⁹, serving as electrode apex models (see Fig. S17). A constrained structural relaxation of the apices and the bridging Pt atoms was performed by keeping the 13 atoms of the base and center layer of each pyramid fixed. The calculation was repeated for several inter-pyramid distances corresponding to junction configurations ranging from compact zigzag to stretched and up to the breaking point of the junction, as seen in Figs. S18a,e. From these calculations, we extracted geometric parameters of the junction (Figs. S18b,c,f,g), including the angles defining the zig-zag structure and the bond lengths within the bridge, as illustrated in Fig. 712. Furthermore, we evaluated the tension developing within the bridge (hereafter termed the force) while pulling the electrodes apart, by forward two-point numerical differentiation of the total energy for a set of relaxed structures of different inter-electrode separations. In this procedure, we first set the inter-electrode separation, then we relax the wire structure while keeping the apex model bases (13 atoms) fixed, and finally we shift both apex bases along the junction's axis to increase the inter-electrodes separation and perform a single-point energy evaluation. The force is evaluated as the numerical derivative of the energy corresponding to the relaxed and stretched configurations with respect to the inter-electrode separation. The resulting force-distance curves appear in Figs. S18d,h. Our calculations show that the Pt atomic wire adopts a linear configuration during stretching (zero zigzag angle) at an early stage before the rupture event (Figs. S18b,f), in agreement with former calculations done for infinite Pt atomic wires⁵. This suggests that a linear wire model is required when studying the wire breaking process.

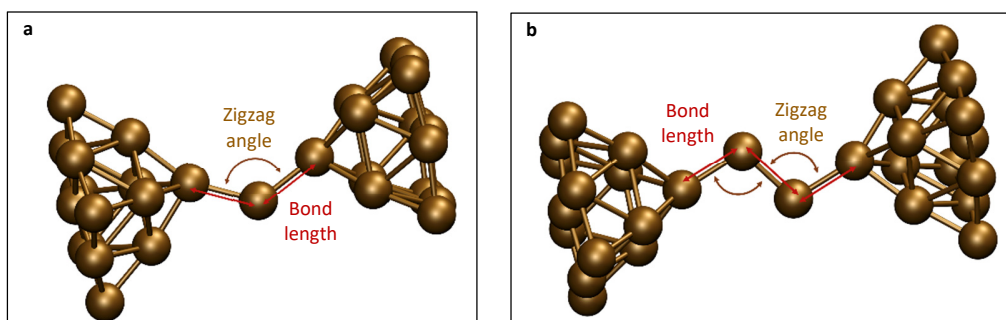


Fig. S17 Schematic representation of 1- and 2- Pt atoms bridging two Pt₁₄ square pyramidal model electrode apices. a, Zigzag angle and bond length for the 1-Pt atom junction used in Figs. S18a-d. **b,** Zigzag angles and bond lengths for the 2-Pt atom junction used in Figs. S18e-h.

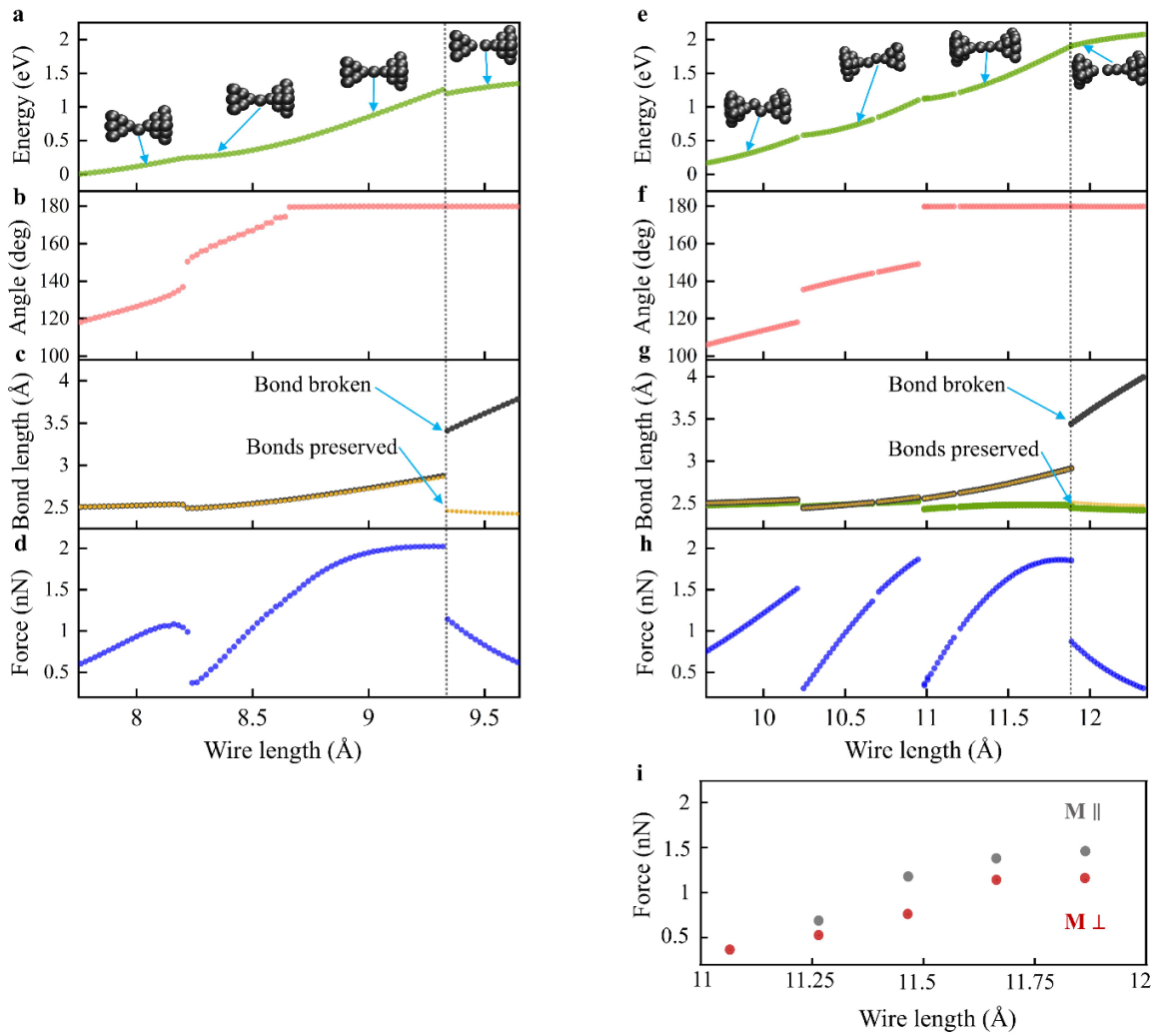


Fig. S18 Zigzag to linear transition and non-collinear spin DFT calculations for Pt atomic wire between electrode apices. Spin-compensated calculations for 1 atom (a-d) and 2 atoms (e-h) bridging the two electrode apex models. **a,e**, Total energy as a function of wire length. **b,f**, Zigzag angle (see Fig. S17) as a function of wire length (inter-electrode separation). In f, the average of the two zigzag angles is presented. **c,g**, Bond length as a function of wire length. An abrupt increase in bond length indicates bond rupture. **d,h**, Force as a function of wire length. The wire is broken at the maximal force. **i**, Non-collinear spin DFT force calculations as a function of wire length for parallel (black) and perpendicular (red) magnetizations (2 atoms bridge is used).

Bare finite atomic wires

Since we are interested in the breaking process, which occurs when the wires are stretched and linear, we next focus on linear wires. In the main text, we have deduced, based on experimental observations, that the force as a function of wire elongation (and hence the total energy curve) depends on the magnetization orientation within the wire. To validate this assumption, we adopted simple, finite linear wire models and performed non-collinear DFT calculations, including spin-orbit interactions, to evaluate the force acting on the wire's edge atoms (prone to rupture, based on our calculations) during wire stretching. This approach extends previous collinear spin

calculations by Thiess *et al.*¹⁰ that compared the elongation tendency of metallic atomic wires in their non-magnetic and (anti)ferromagnetic states. More elaborate non-collinear spin DFT calculations, including explicit electrode apices models are presented below. Since non-collinear spin calculations can lead to multiple solutions with different spin orientations and configurations, we took special care in preparing the starting initial guesses guiding the self-consistent iterations to target solutions with magnetization either perpendicular or parallel with respect to the Pt wire's main axis. We started the non-collinear spin calculations from collinear spin initial guesses with a spin polarization perpendicular and parallel to the wires, for wires of 4-6 equidistant Pt atoms with 3 to 13 unpaired electrons. Once the non-collinear spin calculations converged, we displaced the Pt atoms to a slightly stretched or compressed configuration (with the same number of wire atoms) and performed a new self-consistent calculation using the previous density as a starting guess. To select the solutions that better represent the Pt wire in the presence of electrodes, we discarded solutions with sizable atomic magnetization at the edge atoms⁸.

Figure S14a presents the total energy as a function of length for linear wires of different number of atoms, with magnetization parallel or perpendicular to the wire axis. Our results show that the energy of the stretched wires (beyond equilibrium) is sensitive to the magnetization orientation. Focusing on the wire breaking process, we plot in Figs. 4b,c the calculated force on the peripheral wire atoms during stretching. The force curves for parallel and perpendicular magnetization are clearly different. In view of the distinct energy and force curves for the orthogonal magnetizations, one may expect that the interatomic distance at the breaking point and wire stability during elongation is affected by controlling the magnetization direction in the wire.

Non-collinear spin DFT calculations for Pt atomic wires between electrode apices

To examine the effect of electrode apices on our stretched wire calculations, we selected a few 2-atom junction structures, in the stretched bond region prior to the breaking point, from the zigzag to linear atomic wire transition calculations (described above) and performed non-collinear spin DFT calculations including the spin-orbit interaction for spin magnetizations parallel and perpendicular to the wire's axis. Because the electrodes are not semi-infinite as in the experiments, the magnetization may contaminate the small Pt atomic clusters. Therefore, we took special care to obtain solutions that involve minimal spin polarization on the electrode apices. To this end, we started the non-collinear spin calculations from fragment guesses with closed-shell electrode pyramids and spin polarized bridge atoms with spin orientation parallel and perpendicular to the wire's axis. The resulting force-distance curves are shown in Fig. S18i. For a given wire length, a smaller force is obtained for the perpendicular magnetization orientation than for the parallel one, in line with our results for the bare wire model calculations presented in Fig. S19, supporting the assumptions made in the minimal model described below.

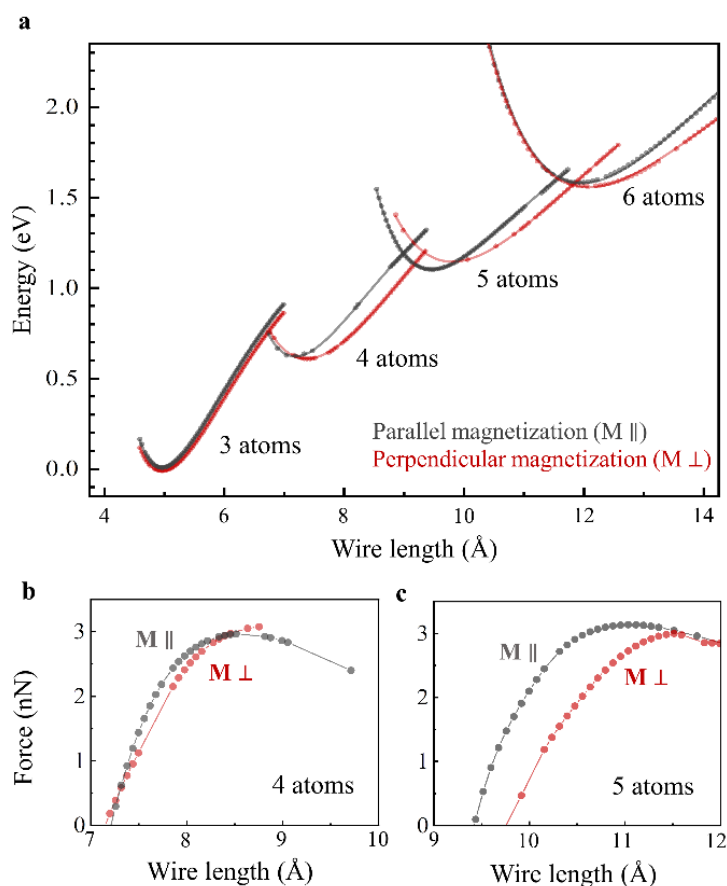


Fig. S19 Non-collinear spin DFT calculations for finite Pt atomic wires. **a**, Total energy as a function of wire length for wires of 3-6 atoms with parallel and perpendicular magnetization. When the wires are stretched beyond the equilibrium length (at minimum energy), the energy versus length dependence is different for the two magnetization orientations. Since emphasis is put on stretched configurations, linear wires are considered, with equal interatomic distance as a simplification. **b,c**, Force on one of the peripheral atoms as a function of wire length for wires composed of 4 (b), and 5 (c) atoms with parallel and perpendicular magnetizations.

Technical details

All DFT calculations were performed with the Gaussian Suite of programs¹¹, using the PBEh hybrid density functional approximation¹²⁻¹⁴. This particular DFT approximation, which admixes 25% of Hartree-Fock exchange with 75% of PBE exchange and 100% PBE correlation, was chosen due to three important features: a) it can be derived from first-principles; b) it admixes orbital-dependent Hartree-Fock type exchange, which has been identified as a necessary component to accurately capture spin-orbit effects¹⁵; and c) it reduces the self-interaction error, which negatively affects density functional calculations involving stretched bonds¹⁶. The Stuttgart-Cologne energy-consistent relativistic (10 electrons) small-core effective core potential, including the spin-orbit component for the non-collinear spin calculations, was employed along with the corresponding aug-cc-pVDZ-PP basis-set¹⁷. A self-consistent convergence criteria of maximal variations of 10^{-6} a.u. in the root mean square density matrix and energy between any two consecutive iterations was employed throughout. No explicit

magnetic field was included in the calculations as it has a negligible effect on the calculated total energies and properties, considering the experimentally relevant magnetic field range of $B \leq 1.5 T$.

Supplementary section 10: Description of the minimal model

A simplified description of the process that takes place in the break-junction experiments presented in this work can be summarized as follows. Initially, two metallic Pt electrodes are pulled apart until a monatomic Pt wire is formed. Upon further pulling apart the electrodes, the wire stretches and can potentially extract another atom from one of the electrodes to form a wire longer by one atom. This will occur provided that the force required for pulling an atom from an electrode does not exceed the force required for wire rupture (maximal force in Fig. 4b of the main text). Providing a fully first-principle description of the wire elongation and rupture processes in the presence of a magnetic field is an intractable problem. Therefore, in order to rationalize the experimental results presented above, we introduce a phenomenological model that captures the main physical aspects of the involved processes. In what follows, we present the essentials of this model.

The basic ingredients and simplifying assumptions of the model are as follows:

1. Out of the intricate manifold of non-collinear spin states that the system has, we consider only two coherent spin states corresponding to magnetization directed in parallel to the wire direction (longitudinal) or perpendicular to it (transverse). This is consistent with the orientation of the external magnetic field relative to the wire axis in the experimental setup. These two extreme magnetization orientations are expected to be the most susceptible to the application of the magnetic field. Other states, such as essentially antiferromagnetic states, are less influenced by the external magnetic field.
2. Since in our experimental setup we focus our attention on wire rupture processes, where the wires are stretched beyond the transition point from zigzag to linear configuration¹⁸, we limit the scope of the rupture model to linear atomic wires, as well. This assumption is supported by the above DFT calculations of the wire's structure during elongation and rupture.
3. Unstretched Pt wires are known to be non-magnetic. Upon stretching, however, magnetism develops^{7,18-20}.
4. Once magnetization arises, its direction remains predominantly unchanged during the entire stretching process up to the wire elongation point, due to an energetic barrier²⁰. See discussion below regarding the height of this barrier.
5. Upon wire elongation, a rapid structural rearrangement occurs, due to the insertion of the additional atom. As a result, the mechanical strain within the wire reduces, leading to near-equilibrium structures and hence suppression of magnetization preference.

6. Wire breaking occurs when the force exerted on its peripheral atoms exceeds the maximal force, which is reached at a different wire length for each magnetization (see Fig. 4b of the main text). This picture is supported by our experimental observations, as well as by ab-initio calculations presented above.
7. In the absence of a magnetic field the wire can adopt either perpendicular or parallel magnetization during stretching. Therefore, when performing many repetitions of the experiment, two distributions of the breaking length will appear for a wire with a given number of atoms, each corresponding to a different magnetization direction. Note that, we assume that in the experiment the separation between the peaks of these two distributions is small, and the distributions of breaking length for a wire with a given number of atoms is seen as a single peak in the experimental length histogram. For the purpose of the present model we assume that these distributions are Gaussian and denote them as $G_t^n(d; d_t^n, \sigma_t) \equiv G_t^n(d)$ and $G_l^n(d; d_l^n, \sigma_l) \equiv G_l^n(d)$ for the perpendicular (transversal) and parallel (longitudinal) magnetization orientations, respectively, where d is the wire length at the breaking point and n is the peak index. Note that to avoid notational confusion between the orientation of the external magnetic field (denoted as perpendicular (\perp) or parallel (\parallel)) and the orientation of the spin magnetization of the wire, we use the terms transversal (t) and longitudinal (l) to describe the perpendicular and parallel magnetization orientations, respectively. With this notation, d_t^n and d_l^n are the mean values of the two distributions of breaking lengths, σ_t and σ_l are their respective widths. The latter are chosen to be $\sigma_t = \sigma_l = 0.5 \text{ \AA}$, which reproduces well the experimental peak width in the length histograms (sensitivity tests against this parameter are shown in Supplementary section 11).
8. Once the magnetic field is switched on, the relative weights of these two distributions change, and the probability to form wires with one magnetization orientation increases, while the probability to form wires with the other magnetization orientation decreases, depending on the direction of the external field. This, in turn, causes the observed shift in the combined peaks envelope that are experimentally observed.

Parallel Magnetic Field

To evaluate the relative probability to adopt one of the two considered magnetization orientations as a function of the magnetic field direction and magnitude as well as the temperature, we assign standard Boltzmann weights to each distribution. For the case of a parallel magnetic field applied along the wire direction (chosen as the z direction here), only longitudinal spin configurations aligned parallel (z) and anti-parallel ($-z$) to the wire axis will be Zeeman shifted by the magnetic field, yielding the following Boltzmann weights:

$$w_{\parallel}^z(B) = e^{\frac{\mu B}{k_B T}},$$

$$w_{\parallel}^{-z}(B) = e^{-\frac{\mu B}{k_B T}},$$

where μ is the effective magnetic moment of the wire (see Supplementary section 9), B is the strength of the magnetic field, and $k_B T$ is the thermal energy. The energetics of the transversal (x and y) spin states remains unaffected by the field resulting in four equivalent spin directions (two, one positive and one negative, along each transversal direction) that are equally populated, giving a total Boltzmann weight of:

$$w_{\parallel}^x(B) = w_{\parallel}^y(B) = 2e^0,$$

where the factor of 2 stands for the two degenerate spin orientations. Using these weights, the overall probability distribution for a wire elongation event to occur as a function of parallel magnetic field intensity and wire length can now be expressed as:

$$D_{\parallel}^n(d; B) = \left[\frac{w_{\parallel}^z(B) + w_{\parallel}^{-z}(B)}{W_{\parallel}(B)} \right] G_l^n(d) + \left[\frac{w_{\parallel}^x(B) + w_{\parallel}^y(B)}{W_{\parallel}(B)} \right] G_t^n(d),$$

where the partition function $W_{\parallel}(B)$ is given by the sum of all unnormalized weights:

$$W_{\parallel}(B) = w_{\parallel}^z(B) + w_{\parallel}^{-z}(B) + w_{\parallel}^x(B) + w_{\parallel}^y(B).$$

The wire $n \rightarrow n + 1$ elongation length is then defined as the peak position, $p_{\parallel}^n(B)$, of the resulting combined distribution $D_{\parallel}^n(d; B)$ for any given magnetic field and temperature. To make direct comparison with the experimental results we then plot the inter-peak distance for the parallel field case:

$$d_{(n+1)-n} = p_{\parallel}^{n+1}(B) - p_{\parallel}^n(B).$$

Perpendicular Magnetic Field

Similarly, when the magnetic field points in a direction perpendicular to the wire axis (chosen as the x direction) we have:

$$w_{\perp}^x(B) = e^{\frac{\mu B}{k_B T}},$$

$$w_{\perp}^{-x}(B) = e^{-\frac{\mu B}{k_B T}},$$

$$w_{\perp}^y(B) = w_{\perp}^z(B) = 2e^0,$$

Then, the overall probability distribution for a wire elongation event to occur as a function of magnetic field and wire length can now be expressed as:

$$D_{\perp}^n(d; B) = \left[\frac{w_{\perp}^z(B)}{W_{\perp}(B)} \right] G_l^n(d) + \left[\frac{w_{\perp}^x(B) + w_{\perp}^{-x}(B) + w_{\perp}^y(B)}{W_{\perp}(B)} \right] G_t^n(d),$$

with the partition function:

$$W_{\perp}(B) = w_{\perp}^x(B) + w_{\perp}^{-x}(B) + w_{\perp}^y(B) + w_{\perp}^z(B).$$

The wire $n \rightarrow n + 1$ elongation length is then defined as the peak position, $p_{\perp}^n(B)$, of the resulting combined distribution $D_{\perp}^n(d; B)$ for any given magnetic field and temperature. To make direct comparison with the experimental results we then plot the inter-peak distance for the perpendicular field case:

$$d_{(n+1)-n} = p_{\perp}^{n+1}(B) - p_{\perp}^n(B).$$

The energy barrier height between parallel and perpendicular wire magnetizations

In the model description, presented earlier in this section, an assumption was made that following elongation, when an atom is inserted into the wire, the wire's strain is partially relaxed and the magnetization preference is suppressed^{7,18-20}, thus facilitating magnetization alignment by a relatively small magnetic field. As the elongated wire is further stretched, parallel and perpendicular magnetization states develop with a corresponding energy barrier separating them (see point number 4 above). To support this picture and demonstrate that the barrier height is larger than the thermal and Zeeman energies under the experimental conditions, we revisit the results of the temperature-dependent experiments appearing in Figs. 4i,j of the main text. Two important observations can be drawn: (i) as discussed in the main text and predicted by our minimal model, the effect of varying the temperature is translated to a change in the saturation magnetic fields (dashed red line in Figs. 4i,j) due to the Boltzmann competition between the thermal and Zeeman energies; and (ii) at any of the three temperatures considered, we find an identical saturation magnetic field for the parallel and perpendicular field orientations. The later observation indicates that the energetic barrier between the two magnetization configurations is larger than the thermal energy in the experiment. To understand this, let us assume that the magnetization barrier is lower than or comparable to the thermal energy. In such a case, starting from the suppressed magnetization state of the partially relaxed elongated wire, the application of a parallel magnetic field favors the parallel magnetization state over its perpendicular counterpart. Elongating the wire will not lead to magnetization locking, due to the low barrier, and thermodynamic considerations will lead to thermal population favoring the lower energy perpendicular magnetization state. To reach saturation with a parallel magnetic field, would then require a very high field strength, beyond the value used in our experiments, that would lower the energy of the parallel magnetization state below that of its perpendicular counterpart. In contrast, to reach saturation with a perpendicular magnetic field, one would need to apply a much lower field strength since the population of the perpendicular magnetization state would be thermodynamically dominating already in the absence of a magnetic field. This would be translated to different saturation field values for the two field orientations at any given

temperature, in contrast to our experimental observations. The fact, that we observe the same parallel and perpendicular saturation fields for the three different temperatures considered, indicates that the barrier height is considerably larger than experimental thermal energy, such that at the experimental timescale there is no thermal drift of population from the less stable longitudinal magnetization state to the energetically favorable transverse magnetization state of the stretched wires. We further note that the Zeeman energy in our experiments is of the order of the thermal energy and therefore also smaller than the barrier height of the stretched wire under the experimental conditions. This, therefore, makes it impossible to affect the wire's magnetization state using magnetic fields, once the wire is stretched.

Supplementary section 11: Model sensitivity with respect to input parameters

Our model includes three free parameters, the elongation distribution width (σ), the magnetic moment of the Pt wire (μ), and the breaking length (d). These parameters are defined in Supplementary section 10. To test the sensitivity of our model outcomes with respect to its input parameters, we repeated the calculations presented in the main text for several values of the distribution width, effective magnetic moment, and the breaking length. As shown below, the qualitative nature of our results is insensitive to the value of these parameters within reasonable physical bounds.

Distribution Width σ

The choice of the widths σ_t and σ_l of the distribution functions $G_t^n(d)$ and $G_l^n(d)$ affects the resulting distributions $D_{\parallel}^n(d; B)$ and $D_{\perp}^n(d; B)$ and thus also the calculated peak positions, $p_{\parallel}^n(B)$ and $p_{\perp}^n(B)$. These widths are used as empirical fitting parameters to obtain good agreement with the experimentally measured peak widths as appearing in the length histograms. In the main text, we presented results obtained using a value of $\sigma_t = \sigma_l = 0.5 \text{ \AA}$. To evaluate the robustness of this choice we repeated the calculations of the inter-peak distance dependence on the magnetic field, using slightly smaller and larger values of $\sigma_t = \sigma_l = 0.4 \text{ \AA}$ and $\sigma_t = \sigma_l = 0.6 \text{ \AA}$, respectively. As can be seen in Fig. S20, the results are weakly sensitive to variations of the width parameters within the range considered, regardless of the magnetization orientation.

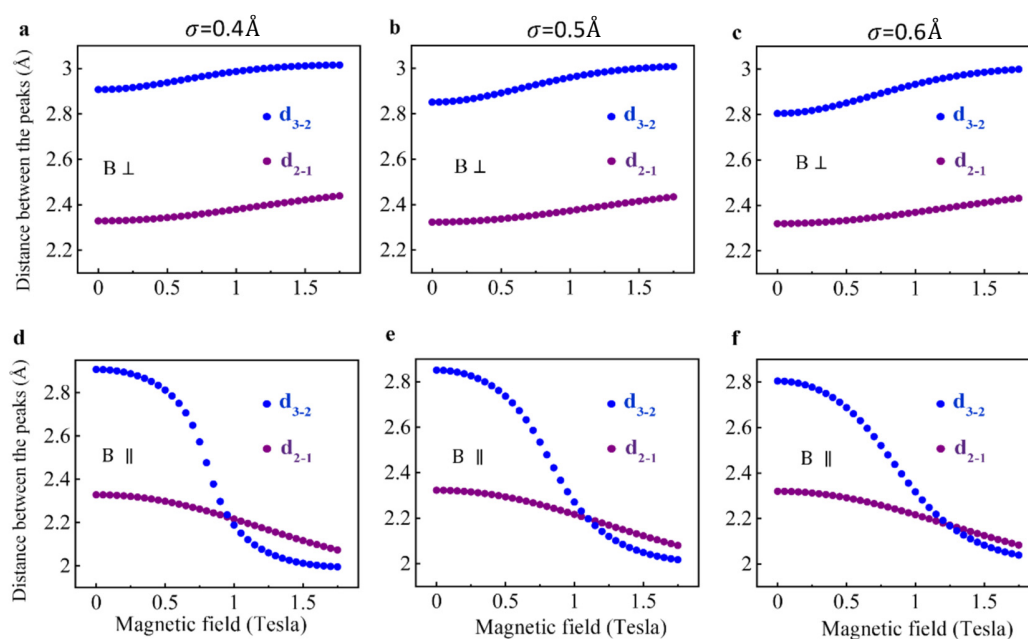


Fig. S20 Model sensitivity test against the peak width parameter. Calculated inter-peak distances as a function of perpendicular (upper panels) and parallel (lower panels) applied magnetic field for $\sigma_t = \sigma_l = 0.4 \text{ \AA}$ (panels a and d), 0.5 \AA (panels b and e), and 0.6 \AA (panels c and f). The calculations are performed using $\mu_0 = 2.5 \mu_B$.

Effective Magnetic Moment μ

The effective magnetic moment that enters in the weight functions discussed above, can be written as $\mu = n \mu_0$, where n is the number of Pt atoms in the wire and μ_0 is the average magnetic moment per atom. This allows us to use the same μ_0 for the different wires as an additional simplification. Comparing the magnetic field dependence of the inter-peak positions obtained from our model with the experimental results, one can estimate the value of $\mu_0 = 2.5 \mu_B$, used to obtain the results presented in the main text. As reference, the magnetic moment of a stretched Pt wire was reported in the literature by several authors. Fernández-Seivane *et al.*⁷ predicted a spin magnetic moment of approximately $1.25 \mu_B$ per Pt atom, using generalized gradient DFT approximation (GGA) calculations on stretched linear and zig-zag wires. Smogunov *et al.*²⁰ estimated a total magnetic moment per Pt atom (with comparable spin and orbital contributions) of approximately $1.5 \mu_B$, using the GGA. Considering that GGA tends to underestimate the calculated magnetic moments²¹, we believe that our estimated value is within reasonable physical bounds. Nonetheless, to assess the robustness of our predictions towards variations in the value of μ_0 , we repeated the calculations of the inter-peak distance dependence on the magnetic field using slightly smaller and larger values of $\mu_0 = 2.0 \mu_B$ and $3.0 \mu_B$, respectively. As can be seen in Fig. S21, the general trend is not affected by varying the effective magnetic moment within the considered range, for both magnetization orientations.

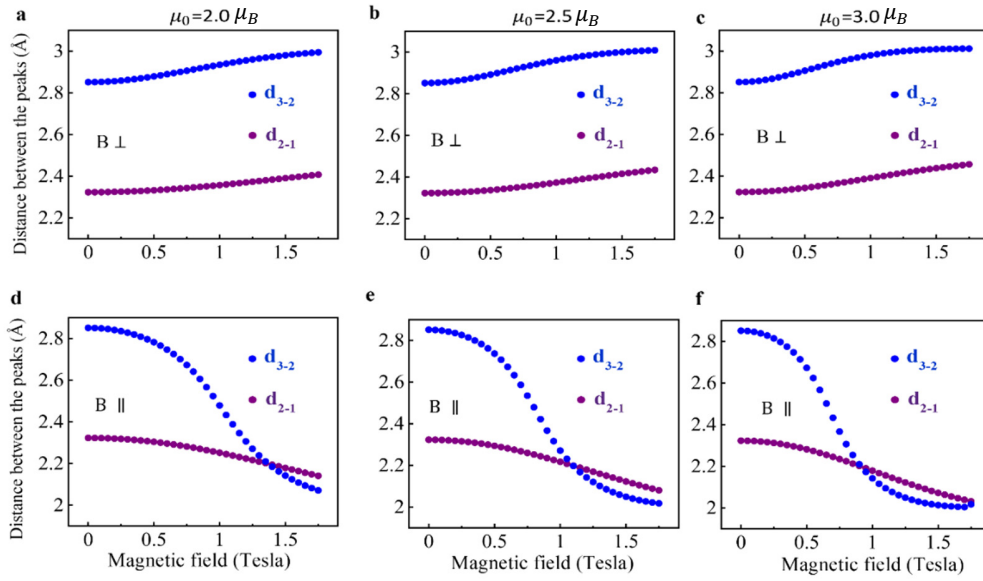


Fig. S21 Model sensitivity test against the effective magnetic moment parameter. Calculated inter-peak distances as a function of applied perpendicular (upper panels) and parallel (lower panels) magnetic field for $\mu_0 = 2.0 \mu_B$ (panels a and d), $2.5 \mu_B$ (panels b and e), and $3.0 \mu_B$ (panels c and f). The calculations are performed using $\sigma = 0.5 \text{ \AA}$.

Breaking length

For a wire with a given number of atoms, the parallel and perpendicular breaking lengths (d_{\parallel} , d_{\perp}) are defined as the stretching lengths at which the force is maximal (see Fig. 4b of the main text). These breaking lengths can be extracted from the experiments by considering the peak positions at saturation ($B > 1.25 \text{ T}$ for Pt atomic wires). In these conditions and at zero temperature, the positions of the peaks provide the breaking length of wires with magnetization along the applied magnetic field. However, at the experimental temperature (5.1 K) this method underestimates the experimental breaking lengths by roughly 20% due to the thermal energy competition with the Zeeman energy. To check the sensitivity of the model results with respect to the values of the breaking lengths, we present in Fig. S22 the calculated inter-peak distance dependence on the magnetic field strength using breaking lengths increased by 10% and 20%, with respect to that used in Fig. 4. The overall quantitative behavior is found to be only mildly sensitive to the value of the breaking length with no influence on the qualitative nature of the results.

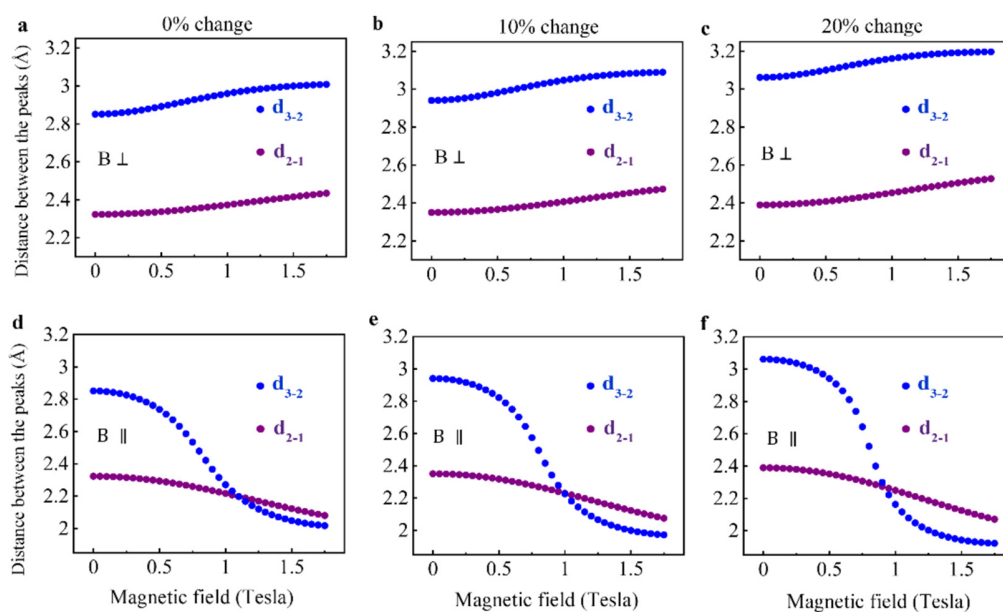


Fig. S22 Model sensitivity test against the breaking length. Calculated inter-peak distances as a function of applied perpendicular (upper panels) and parallel (lower panels) magnetic field for the obtained breaking length based on the saturation location of the peaks (a,d), and larger breaking length values by 10% (b,e) and 20% (c,f). The calculations are performed using $\sigma = 0.5 \text{ \AA}$ and $\mu_0 = 2.5 \mu_B$.

Supplementary section 12: Temperature dependent measurements

The effect of magnetic field on the inter peak distance measured at different temperatures is presented in Fig. S23.

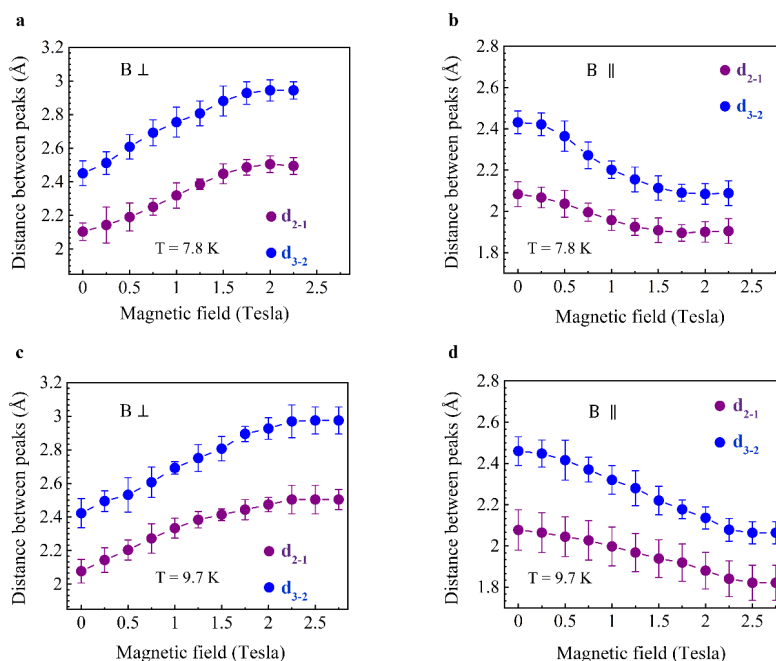


Fig. S23 Magnetic-field-induced structural variations in Pt atomic wires. Inter-peak distance as a function of perpendicular (a,c) and parallel (b,d) magnetic fields at 7.8 K (a,b) and 9.7 K (c,d).

Supplementary section 13: Absence of hysteresis

In contrast to magnetostriction measurements, in our experiments no hysteresis is expected because of the following: (i) An insignificant magnetization preference whenever an atom is inserted to the wire and the interatomic distance is partially relaxed^{7,18-20}, as supported by the relatively low involved magnetic fields (~ 1 T). (ii) Lack of memory between different wire elongation events. Namely, we compare independent wires that are formed under different magnetic field orientations. Before the formation and characterization of any given wire, we crash the two electrodes into each other to form a contact of about 70-100 atoms to allow the independent formation of a new wire without being affected by past induced magnetic fields and the structure of former wires.

References

1. Strigl, F., Espy, C., Bückle, M., Scheer, E. & Pietsch, T. Emerging magnetic order in platinum atomic contacts and chains. *Nat. commun.* **6**, 1-9 (2015)
2. García-Suárez, V. M., Rocha, A. R., Bailey, S. W., Lambert, C. J., Sanvito, S. & Ferrer, J. Conductance oscillations in zigzag platinum chains. *Phys. Rev. Lett.* **95**, 256804 (2005)
3. Vardimon, R., Yelin, T., Klionsky, M., Sarkar, S., Biller, A., Kronik, L. & Tal, O. Probing the orbital origin of conductance oscillations in atomic chains. *Nano Lett.* **14**, 2988-2993 (2014)
4. Yelin, T., Vardimon, T., NKuritz, N., Korytár, R., Bagrets, A., Evers, F., Kronik, L., & Tal, O., Atomically Wired Molecular Junctions: Connecting a Single Organic Molecule by Chains of Metal Atoms, *Nano Lett.* **13**, 1956–1961 (2013)
5. R. H. M. Smit, C. Untiedt, A. I. Yanson, and J. M. van Ruitenbeek, Common Origin for Surface Reconstruction and the Formation of Chains of Metal Atoms, *Phys. Rev. Lett.* **87**, 266102 (2001)
6. R. H. M. Smit, C. Untiedt, G. Rubio-Bollinger, R. C. Segers, and J. M. van Ruitenbeek, Observation of a Parity Oscillation in the Conductance of Atomic Wires, *Phys. Rev. Lett.* **91**, 076805 (2003)
7. Fernández-Seivane, L., García-Suárez, V. M. & Ferrer, J. Predictions for the formation of atomic chains in mechanically controllable break-junction experiments. *Phys. Rev. B* **75**, 075415 (2007)
8. Smogunov, A., Dal Corso, A. & Tosatti, E. Magnetic phenomena, spin-orbit effects, and Landauer conductance in Pt nanowire contacts: Density-functional theory calculations. *Phys. Rev. B* **78**, 014423 (2008)
9. Wei G. F. & Liu Z. P. Subnano Pt Particles from a First-Principles Stochastic Surface Walking Global Search, *J. Chem. Theory and Comput.* **12**, 4698–4706 (2016)
10. Thiess, A., Mokrousov, Y., Heinze, S. & Blügel, S. Magnetically hindered chain formation in transition-metal break junctions. *Phys. Rev. Lett.* **103**, 217201 (2009)
11. Gaussian 16: Gaussian 16, Revision B.01, Frisch, M. J., *et al.*, Gaussian, Inc., Wallingford CT (2016)
12. Perdew, J. P., Ernzerhof, M. & Burke, K. Rationale for Mixing Exact Exchange with Density Functional Approximations. *J. Chem. Phys.* **105**, 9982-9985 (1996)
13. Ernzerhof, M. & Scuseria, G. E. Assessment of the Perdew-Burke-Ernzerhof Exchange-Correlation Functional. *J. Chem. Phys.* **110**, 5029-5036 (1999)
14. Adamo, C. & Barone, V. Toward Reliable Density Functional Methods without Adjustable Parameters: The PBE0 Model. *J. Chem. Phys.* **110**, 6158-6170 (1999)
15. Desmarais, J. K., Flament, J. P. & Erba, A. Fundamental Role of Fock Exchange in Relativistic Density Functional Theory. *J. Phys. Chem. Lett.* **10**, 3580-3585 (2019)
16. Shahi, C., Bhattarai, P., Wagle, K., Santra, B., Schwalbe, S., Hahn, T., Kortus, J., Jackson, K. A., Peralta, J. E., Trepte, K. & Lehtola, S. Stretched or noded orbital densities and self-interaction correction in density functional theory. *J. Chem. Phys.* **150**, 174102 (2019)
17. Figgen, D., Peterson, K. A., Dolg, M. & Stoll H. Energy-consistent pseudopotentials and correlation consistent basis sets for the 5d elements Hf-Pt. *J. Chem. Phys.* **130**, 164108 (2009)
18. Tung, J. C. & Guo, G. Y. Magnetic moment and magnetic anisotropy of linear and zigzag 4 d and 5 d transition metal nanowires: First-principles calculations. *Phys. Rev. B* **81**, 094422 (2010)
19. Delin, A. & Tosatti, E. Magnetic phenomena in 5 d transition metal nanowires. *Phys. Rev. B* **68**, 144434 (2003)
20. Smogunov, A., Dal Corso, A., Delin, A., Weht, R. & Tosatti, E. Colossal magnetic anisotropy of monatomic free and deposited platinum nanowires. *Nat. Nanotechnol.* **3**, 22-25 (2008)
21. Fernández-Rossier, J., Jacob, D., Untiedt, C. & Palacios, J. J. Transport in magnetically ordered Pt nanocontacts. *Phys. Rev. B* **72**, 224418 (2005)